

HAROKOPIO UNIVERSITY

School of Environment, Geography and Applied Economics



Department of Geography

Postgraduate Program

“Applied Geography and Spatial Planning”

Stream C: Geoinformatics

**«Monitoring impacts of climate change on surface subsidence using SAR
Interferometry after the activation of Karla lake reservoir for water-consuming
control for irrigation»**

Postgraduate thesis

Karavias Andreas

Athens, March 2021

HAROKOPIO UNIVERSITY

School of Environment, Geography and Applied Economics



Department of Geography

Postgraduate Program

“Applied Geography and Spatial Planning”

Stream C: Geoinformatics

Three member Committee:

Isaak Parcharidis (Supervisor)

Assistant Professor, Department of Geography, Harokopio University

Francesca Cigna

Senior researcher in Earth Observation, Institute of Atmospheric Sciences and

Climate (ISAC), National Research Council (CNR) of Italy

George Petropoulos

Assistant Professor in Geoinformation, Department of Geography, Harokopio

University of Athens

Athens, March 2021

Ο Καραβίας Ανδρέας

δηλώνω υπεύθυνα ότι:

1. Είμαι ο κάτοχος των πνευματικών δικαιωμάτων της πρωτότυπης αυτής εργασίας και από όσο γνωρίζω η εργασία μου δε συκοφαντεί πρόσωπα, ούτε προσβάλλει τα πνευματικά δικαιώματα τρίτων.
2. Αποδέχομαι ότι η ΒΚΠ μπορεί, χωρίς να αλλάξει το περιεχόμενο της εργασίας μου, να τη διαθέσει σε ηλεκτρονική μορφή μέσα από τη ψηφιακή Βιβλιοθήκη της, να την αντιγράψει σε οποιοδήποτε μέσο ή/και σε οποιοδήποτε μορφότυπο καθώς και να κρατά περισσότερα από ένα αντίγραφα για λόγους συντήρησης και ασφάλειας.

To my beloved grandfather (a fisherman of Karla lake).

ACKNOWLEDGEMENTS

I would like to thank Professor Issaak Parcharidis for his help and for the knowledge that I gained through my collaboration with him. Moreover, I would like to thank Dr. Francesca Cinga and Dr. Deodato Tapete for their guidance and help that provided me about the process of Como-SkyMed data and general knowledges about multi-temporal DInSAR methods. Also, I want to thank Athanasia-Maria Tompolidi for her great support and Pavlos Krassakis for providing geological data. Finally, my family and my colleagues who were by my side all this time, believed in me and help me to achieve my goals.

Table of contents

Περίληψη.....	7
Abstract.....	8
1. Introduction.....	13
2. Study Area.....	15
2.1 Case study.....	15
2.2 Human Geography.....	17
2.3 Land uses and exposure.....	18
2.4 Physical Geography - Geology.....	19
2.5 Climate of Larissa Plain.....	24
3. Climate Change.....	25
4. Literature Review.....	27
5. Basic Principles.....	31
5.1 Radar.....	31
5.2 SAR Satellites.....	33
5.2.1 SAR Acquisition Geometry.....	34
5.2.3 Interaction of SAR signal with the earth's surface.....	35
.....	35
5.2.4 SAR Characteristics.....	36
5.3 Copernicus Programme.....	38
5.4 Satellites systems.....	39
5.4.1 Copernicus program-Sentinel 1 constellation.....	39
5.4.2 COSMO-SkyMed.....	42
5.5 Interferometric Synthetic Aperture Radar.....	44
5.5.1 Differential Interferometry (DinSAR).....	49
5.5.2 Multi-temporal InSAR.....	50
5.5.3 The SBAS Approach.....	51
6. Data and Methodology.....	53
6.1 Data.....	53
6.2 Methodology.....	54
7. Results.....	61
8. Discussion - Conclusion.....	81
Reference.....	84
Appendix.....	88

Περίληψη

Η εδαφική καθίζηση είναι ένας κίνδυνος ο οποίος επηρεάζει πολλές περιοχές σε όλο τον κόσμο και μπορεί να έχει σημαντική επίδραση τόσο στο ανθρωπογενές όσο και στο φυσικό περιβάλλον. Ένας από τους κύριους παράγοντες εμφάνισης αυτού του φαινομένου είναι η μείωση των αποθεμάτων των υπόγειων υδάτων, η οποία οφείλεται κατά κύριο λόγο στην άντληση νερού για αγροτικές δραστηριότητες και της κλιματικής αλλαγής με την μείωση των βροχοπτώσεων. Η συνεχή άντληση του νερού σε συνδυασμό με την κλιματική αλλαγή οδηγεί στην σημαντική μείωση των αποθεμάτων του υπόγειου νερού με αποτέλεσμα την εμφάνιση έντονης καθίζησης. Η εργασία αυτή εστιάζει στο νότιο τμήμα της πεδιάδας της Λάρισας η οποία αποτελεί χαρακτηριστικό παράδειγμα αυτού του φαινομένου. Στο νότιο τμήμα της πεδιάδας υπήρχε η λίμνη Κάρλα η οποία αποξηράνθηκε το 1962 και η έκτασης μετατράπηκε σε καλλιεργήσιμη γη. Καθώς οι ανάγκες για νερό αυξήθηκαν και τα επιφανειακά ύδατα δεν αρκούσαν για να καλύψουν τις ανάγκες της περιοχής, ξεκίνησαν οι ανεξέλεγκτες γεωτρήσεις με αποτέλεσμα την ταχύτερη μείωση των υπόγειων υδάτων. Οι γεωτρήσεις αυτές, οδήγησαν στην μεγαλύτερη εμφάνιση καθιζήσεων στις γύρω περιοχές με καταγραφές ζημιών σε κτίρια και δρόμους. Μετά από πίεση των τοπικών αρχών, το 2010 ξεκίνησε το γέμισμα της λίμνης με σκοπό την αντιμετώπιση του προβλήματος το οποίο είχε προκληθεί. Από τότε, έχουν γίνει αρκετές μελέτες από ερευνητές οι οποίοι χρησιμοποιούν μεθόδους δορυφορικής τηλεπισκόπησης αξιοποιώντας δεδομένα ραντάρ, έχοντας ως στόχο να εξετάσουν την ταχύτητα καθίζησης της περιοχής με ακρίβεια εκατοστών. Η εργασία έρχεται να αναβαθμίσει τις υπάρχουσες μελέτες οι οποίες έχουν πραγματοποιηθεί για την πεδιάδα της Λάρισας για την χρονική περίοδο του 2015-2020. Για την εκπόνηση της εργασίας χρησιμοποιήθηκαν DInSAR τεχνικές, αξιοποιώντας 315 SAR εικόνες από τα δορυφορικά συστήματα Sentinel-1 και COSMO-SkyMed με σκοπό την καταγραφή της καθίζησης, εφαρμόζοντας τεχνικές αποσύνθεσης της παραμόρφωσης έτσι ώστε να υπολογιστεί η κάθετη και οριζόντια κίνηση της περιοχής. Για την επεξεργασία και την οπτικοποίηση των αποτελεσμάτων χρησιμοποιήθηκαν τα ιδιωτικά λογισμικά SARscape 5.5 v ENVI και ArcGIS. Τέλος για την επαλήθευση των αποτελεσμάτων, αξιοποιήθηκαν δεδομένα GNSS καθώς και μετεωρολογικά δεδομένα για την ερμηνεία των εποχικών μεταβολών της καθίζησης.

Λέξεις κλειδιά: Συμβολομετρία, νότια πεδιάδα της Λάρισας, καθίζηση, λίμνη Κάρλα, ραντάρ

Abstract

Land subsidence is a problem that affects many areas around the world and can cause significant damage to the human and natural environment. One of the main causes of this phenomenon is the reduction of groundwater reserves which is mainly caused by the irrigation of water for agricultural activities. The continuous pumping of water in combination with climate change leads to a significant reduction in groundwater reserves resulting in a strong occurrence of subsidence. This thesis focuses on the southern Larissa plain which is a typical example of this phenomenon. In the southern part of that plain, there was existed Lake Karla which dehydrated in 1960 and the area was converted into arable land. As water needs increased and surface water reserves were not enough to cover all needs of the area, uncontrolled drilling began resulting in faster groundwater depletion. These drillings, in combination with periods of intense drought, led to the intense occurrence of land subsidence in the surrounding areas with reports of damaged buildings and roads. In 2010, under the pressure of local authorities, started the recharge of Karla lake in order to minimize the effects of the phenomenon. Since then, several studies have been conducted by authors applying satellite remote sensing methods using Radar data to investigate the subsidence trends of the area with an accuracy of centimeters. This study aims to update the already existing studies and to examine if there is a change in the subsidence trends of the area after the recharge of Karla lake during the period 2015-2020. InSAR techniques will be applied by using 315 SAR images of satellites Sentinel-1 and COSMO-SkyMed to observe the velocity trend, applying deformation decomposition techniques to calculate vertical and horizontal movement. Commercial software SARscape 5.5 v ENVI and ArcGIS were used to generate and visualize the results. Finally, for the validation of the results, GNSS data were used as well as meteorological data to interpret the seasonal changes of subsidence rates.

Keywords: Interferometry, subsidence, southern Larissa plain, Karla lake, SAR

Figures

Figure 1: Location map of Greece and zoom-in the study area of the broader area of southern Larissa plain.....	15
Figure 2: Lake Karla before (2008) and after recharge.....	16
Figure 3: Land cover for SE Thessaly plain (Corine Land Cover 2018).....	18
Figure 4: Geological map of the eastern plain of Thessaly ,source :Institute of Geology and Mineral Exploration (IGME). Contains modified Sentinel-2 copernicus data as basemap.....	20
Figure 5: Simplified structural map of eastern Thessaly showing the major normal faults activated during the Pliocene-Lower Pleistocene extensional régime which generated the NW-SE trending Larissa Basin (Caputo <i>et al.</i> 1994).....	21
Figure 6: Graph of groundwater withdrawal versus time at a borehole at Niki village area. Mean water level drop measured from the ground surface is about 51 m in 20 years (1981–2001) (Kontogianni <i>et al.</i> 2007).....	22
Figure 7: Graph of groundwater withdrawal versus time at a borehole at five settlements of Gitroni, Chalki, Platiampos, Kipseli(Kileler) and Niki for time period of 1985-2004. Modified Polyzos <i>et al.</i> 2006.....	23
Figure 8: Meteorological Data of Larissa Plain 2015-2020. Blue bars representing rainfall and red lines the mean temperature of every month.....	24
Figure 9: SAR geometry acquisition (Henschel <i>et. al.</i> , 2016).....	34
Figure 10: : X, C & L bands penetration (ESA).....	35
Figure 11: Sentinel-1 spacecraft (ESA, 2012).....	39
Figure 12: Cosmo-skymed spacecraft.....	43
Figure 13: PS and DS scatterers.....	52
Figure 14: Connection graph showing perpendicular and temporal baselines of SLC pairs relative to the master image: (Left) Sentinel-1 Ascending mode (master: 30 July 2020), (Right) Sentinel-1 Descending mode (master: 25 February 2020).....	56
Figure 15: Connection graph showing perpendicular and temporal baselines of SLC pairs relative to the master image for COSMO – SkyMed data in Ascending mode (master: 14 May 2020), (Left) 2D connection, (Right) triangulation connection.....	57
Figure 16: Coherence maps for ascending(left) and descending(right) geometry of Sentinel-1...	59
Figure 17: Time series plot for reference point ascending(top) and descending(down).....	60
Figure 18: Average deformation trend for Ascending Sentinel-1.....	61
Figure 19: Average deformation trend for Descending Sentinel-1.....	62
Figure 20: Cross sections in Ascending mode using Sentinel-1 products.....	63
Figure 21: Deformation Time Series from SBAS using Sentinel-1 data between Mar-2015 and 22-Oct -2020 over Thessaly plain,Greece.....	64
Figure 22: Average deformation trend on Vertical after displacement decomposition of two geometries for Sentinel-1 data.....	65
Figure 23: Average deformation trend on East-West after displacement decomposition of the two geometries using Sentinel-1 data.....	66
Figure 24: Bar plot showing the mean average subsidence trend for the five main settlements of study area.....	67
Figure 25: Comparison of cumulative times-series on vertical displacement with GNSS station in Stefanovikio(STEF).....	68
Figure 26: Barplot showing the change of high values of subsidence trend by comparing results of this thesis with a previews research on the same area.....	69
Figure 27: Comparison of cumulative deformation from PS(ALOS PALSAR 2007-2011) and SBAS (Sentinel-1 2015-2020) data. The image contains modified data of Benekos <i>et al.</i> 2014..	70
Figure 28: Map of average deformation trend in ascending mode based on CSK data.....	71

Figure 29: Histograms for the three biggest settlements.....	72
Figure 30: Comparison of mean subsidence rate between five settlement using Sentinel-1 and CSK products.....	73
Figure 31: Map of Stefanovikio settlement with the location of scatterers that used for the correlation of subsidence/rainfall.....	74
Figure 32: Time-Series plot of cumulative subsidence on Stefanovikio settlement (up). Cumulative times series correlated with rainfall data (down).....	75
Figure 33: Scatter plot of rainfall-cumulative subsidence of dry-wet seasons during the period 2015-2020 of Sentinel-1 vertical displacement product after displacement decomposition.....	76
Figure 34: Subsidence rate difference between Dry – Wet season of every year for Sentinel-1. The highest difference is detected in 2019 (up to 33 mm).....	77
Figure 35: Time-Series plot of cumulative subsidence on Stefanovikio settlement (up).Cumulative times series correlated with rainfall data(down).....	77
Figure 36: Time series of four settlements of Stefanovikio, Kileler, Niki and Armenio. The scatterers are located in areas with high subsidence trends.....	78
Figure 37: Scatter plot of rainfall-cumulative subsidence of dry-wet seasons during the period 2015-2020 CSK vertical displacement product generated by ascending geometry.....	79
Figure 38: Comparison of CSK /Sentinel-1 subsidence rates, correlated with rainfall data covering the same period (Aug 2019 – Oct 2020).....	80
Figure 39: Locations of scatterers of CSK data that used for time-series plots.....	95

List of tables

Table 1: Table showing the frequency and wavelength of every band in microwave spectrum....32

Table 2: COSMO-SkyMed launch dates.....42

Table 3: COSMO-SkyMed specific operating mode profile.....43

Table 4: Separation of months on dry - wet seasons based on precipitation. Cumulative subsidence and rainfall is calculated the for every season during the period 2015-2020 of Sentinel-1 vertical displacement product after displacement decomposition.....76

Table 5: Separation of months on dry - wet seasons based on precipitation. Cumulative subsidence and rainfall is calculated the for every season during the period 2019-2021 of CSK vertical displacement product generated by ascending geometry.....78

Abbreviations

AOI	Area of interest
CLC	Corine Land Cover
CSK	Cosmo - SkyMed
DInSAR	Differential SAR Interferometry
DEM	Digital Elevation Model
ESA	European Commission
GNSS	Global Navigation Satellite System
GIS	Geographical Information System
LOS	Line of sight
InSAR	Interferometric synthetic aperture radar
SAR	Synthetic Aperture Radar
SBAS	Small Baseline Subset
SLC	Slant-range single-look complex
SRTM	Shuttle Radar Topography Mission
USGS	United States Geological Survey

1. Introduction

Land subsidence is a gradual settling or sudden sinking of the Earth's surface due to the removal or displacement of subsurface earth materials. One of the principal causes is the aquifer-system compaction associated with groundwater withdrawals. When large amounts of groundwater have been withdrawn from certain types of rocks, such as fine-grained sediments. The rock compacts because the water is partly responsible for holding the ground up. When the water is withdrawn, the rocks fall in on themselves. Where groundwater depletion is involved, subsidence is typically gradual and widespread (USGS).

Remote sensing is a tool that can be used to detect and map land-surface deformation. The method is known as interferometric synthetic aperture radar (InSAR). InSAR uses repeat-pass radar images from Earth-orbiting satellites to monitor subsidence and uplift in incredible detail. Once subsidence is identified and mapped, assessments of the InSAR data can be done to improve our understanding of the subsidence processes. A combination of scientific understanding and careful natural-resource management can minimize the subsidence that results from developing our land and water resources (USGS). Multitemporal InSAR methods using a big number of radar satellite images, it is the only tool that can use information from previous years in order to generate maps that showing the deformation rates over a small or big scale areas with a low cost of resources.

This study focuses on the southern Thessaly plain which is located geographically in central Greece and has been studied by several researchers due to high trends of land subsidence. The aim of the study is to update the previous investigations (Parcharidis *et al.* 2011, Benekos *et al.* 2014, Fouvelis *et al.* 2016) about subsidence, due to overpumping and drought, occurred in the area after the recharge of the lake Karla and verifying or not the phenomenon of deceleration probability. Specifically, we attempt to measure seasonal deformation and its spatial distribution. Displacement maps of the high spatial resolution were generated for the southern Larissa Plain using Synthetic Appearance Radar (SAR) acquisitions from Sentinel-1 and COSMO-SkyMed satellites. The processing of SAR data is based on commercial SARscape(5.5v) ENVI software and the visualization of final products on Geographic Information System(GIS) environment on commercial ArcGIS software.

The master thesis consists of seven main chapters which analyze and explain the use and interpretation of multi-temporal interferometry, as listed below:

Chapter 1: "Study Area " which are analyzed the main characteristics of the area such as the case study, geology, human geography, land uses, and exposure.

Chapter 2: "Climate Change" describing the phenomenon and explaining the correlation with subsidence.

Chapter 3: "Literature Preview" in which referred other studies and authors with similar methods and goals.

Chapter 4: "Basic principles" which are referred general theoretical bases of earth observation Radar systems and the Interferometric principles

Chapter 5: "Data and Methodology" which are referred the SAR SLC dataset, the meteorological data, and the methods that were used for the generation of subsidence maps using the SBAS algorithm in SARscape software.

Chapter 6: "Results" in which are presented the surface subsidence maps analyzed on ArcGIS and time series plots in order to observe the patterns of subsidence in the study area.

Chapter 7: "Conclusions- Discussion" which are presented the conclusions of this master thesis and discussed ideas for future research in the area of southern Larissa plain.

2. Study Area

2.1 Case study

Our study area focuses at the southern part of the eastern Thessaly plain (Figure 1). Lake Karla is located at the SE part of the plain of eastern Thessaly plain. It was drained in 1962 to provide cultivated land and to protect surrounding farmlands from flood events. The extensive agricultural activities have lead to increased water demands, which are usually fulfilled by the exploitation of ground-water resources.

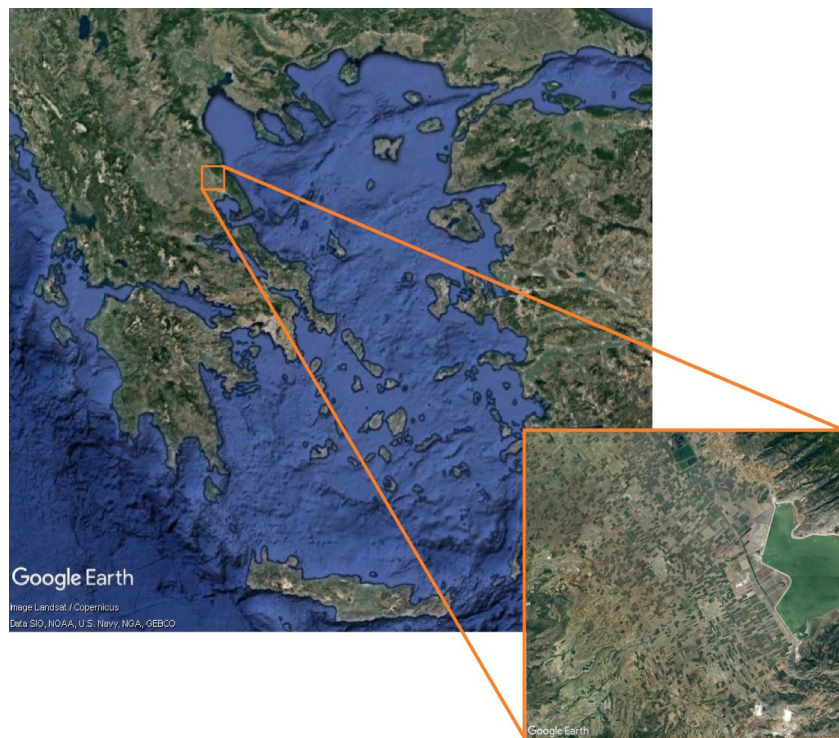


Figure 1: Location map of Greece and zoom-in the study area of the broader area of southern Larissa plain

Since surface water could not cover such needs, thousands of uncontrolled drill holes and wells were bored for water pumping in the last 30 years (Kontogianni *et al.* 2006). The increased water demand is related to severe and persistent droughts during the period from the mid to late 1970s and the period from late 1980s to mid-1990s, interrupted by the wet 1990-1991, which mostly affected the northern part of Thessaly Basin (Loukas *et al.* 2004). A result of dry conditions leads to irrigation cutbacks and the over-exploitation of ground-water. The consequence of these activities was the rapid fall of groundwater which provoked high rates of subsidence as previous research show. The subsidence phenomenon caused damages to

buildings in the area. Field observations made by the authors identified subsidence-induced ground fissures in locations like Larissa-Airport, Kambos, Nikea and Melia villages (Parcharidis *et al.* 2011).

According to Management Body of the Karla Eco-Development Area, strong protests by the local authorities, it was the decision to construct a 42,000-acre reservoir in the lower part of the former Karla Lake near the village of Kanalia. In 2010 started the refilling and the generation of the new Karla lake aiming the rise of the underground aquifers and the restoration of the water potential. The results of this operation are expected to be:

- The rise of the underground aquifer and the restoration of water potential
- Limiting the depletion of groundwater aquifers by supplying water for irrigation
- Improving water quality
- Protection of the Pagasitic Gulf due to the flood purpose of the reservoir and the improvement of the overflowing waters
- Retreat of the seawater front that has penetrated the soil layer of the Pagasitikos and has affected the aquifers
- Partial restoration of the microclimate of the area
- Partial restoration of the flora and fauna of the area

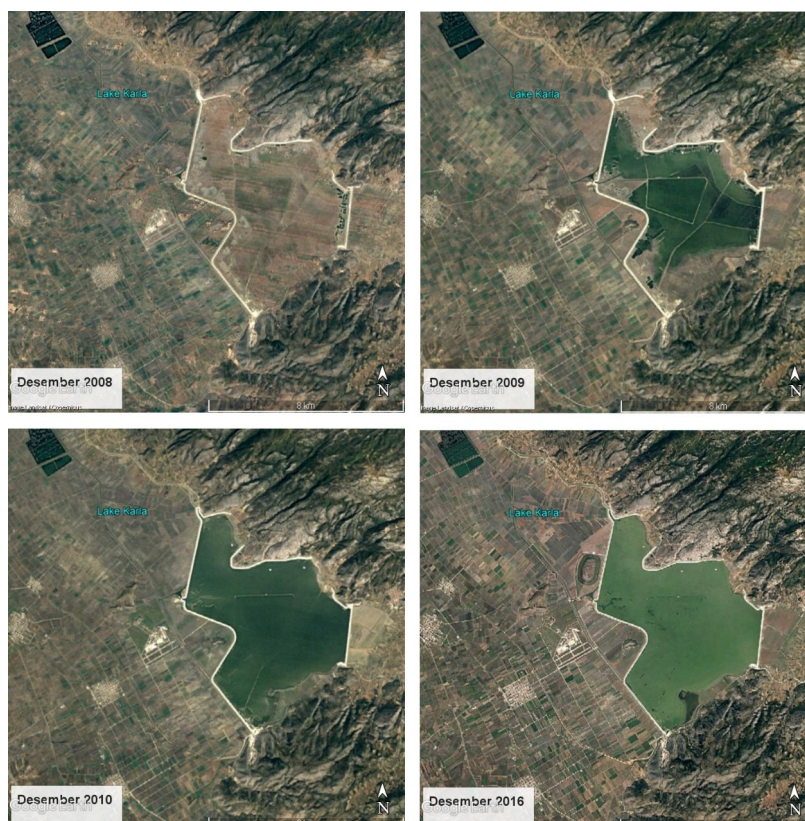


Figure 2: Lake Karla before (2008) and after recharge.

Although ground subsidence is expected to continue. Since then, many studies from authors investigate the spatial and temporal patterns of ground deformation at Eastern Thessaly Plain based on advanced Multitemporal InSAR analysis in order to observe the surface subsidence trend.

2.2 Human Geography

The settlements of the southern Larissa plain such as Stefanovikeio and Rizomyloi, having a large percentage of the inhabitants engaged in agriculture and animal husbandry at a rate. This is followed by the trade and manufacturing. The lowest rates are in services and education. The largest percentage of residents are employed, in contrast to Stefanovikeio where most are self-employed. Most of the self-employed in Rizomylos are in the field of agriculture and animal husbandry. Regarding the level of education, the largest percentage of the inhabitants of the settlements have a high school diploma, while very few are those who have studied in higher education. In conclusion, the main occupation of the settlements is agriculture and animal husbandry.

Before the drying up of Lake Karla (1962) the inhabitants of the surrounding villages lived mainly from fishing. Sources say that more than 1,000 people were fishing in the lake. Karla's drainage brought about socio-economic changes in the settlements, recognizing an adaptation of people with a strong fishing tradition to the new environment, a change in productive activities and an economic decline causing an increased wave of astyphilia. These people actually became farmers. The land distribution of the dried lake was not done under strict institutional frameworks, with the result that many fishermen remained unemployed without being given some land. A large percentage of the inhabitants emigrated to Athens, Thessaloniki, but also abroad. The percentage that emigrated was about 30% and mainly fishermen, 40% turned to agriculture, 20% became industrial workers in Volos, while 10% were engaged in animal husbandry (Ambrazi I., 2009).

2.3 Land uses and exposure

As mentioned above, the main activities of the settlements are agricultural activities, as a result, most of the study area is characterized as arable land (Figure 3).

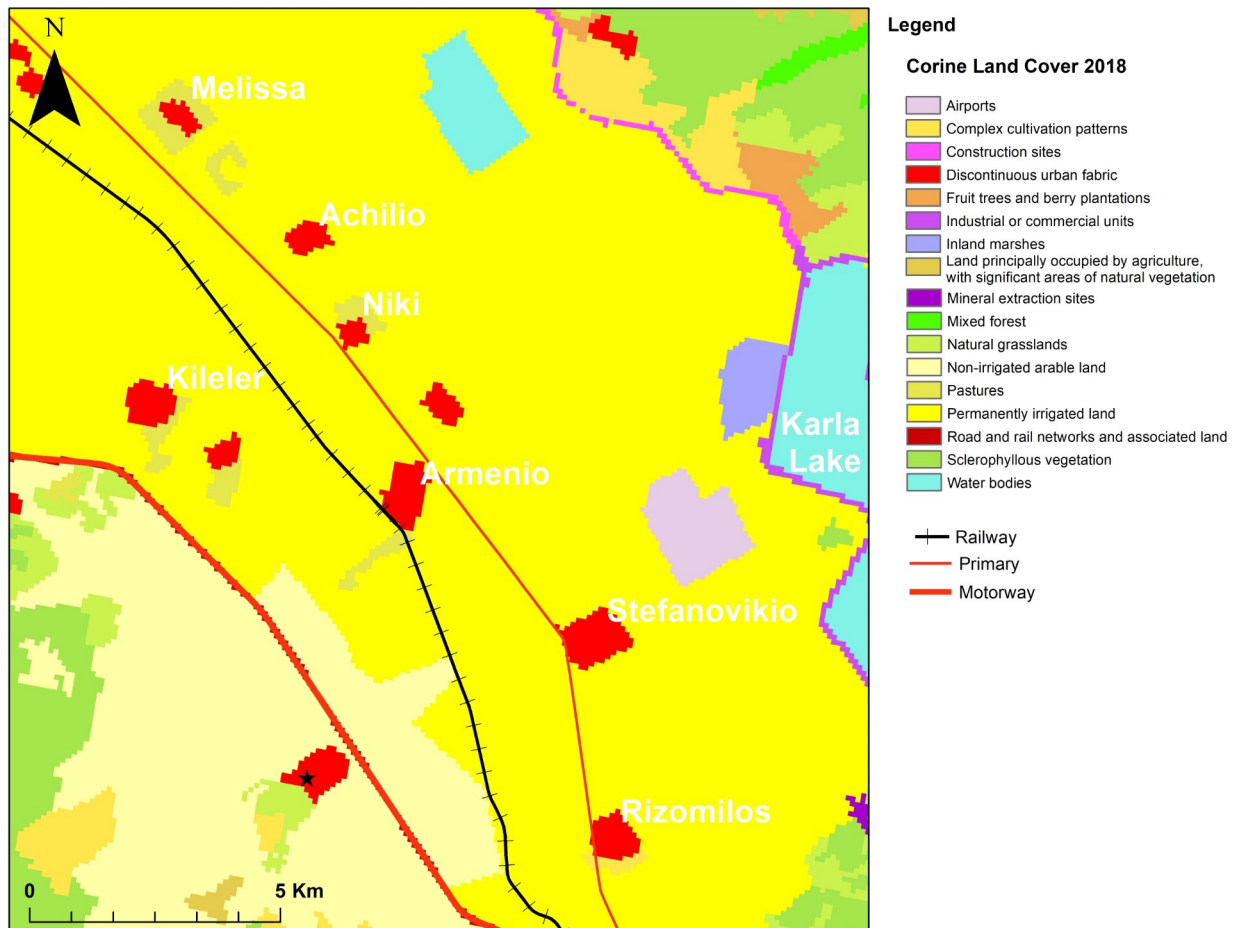


Figure 3: Land cover for SE Thessaly plain (Corine Land Cover 2018).

The settlements in the plain are connected to each other by the main road network. Settlements are expected to have critical infrastructures such as schools and health centers, but unfortunately, our database does not have this geospatial data, suggesting further study in areas where the subsidence trend is high. As we see in the Figure 3, our study area seems to be crossed by a railway that connects the city of Larissa with Volos as well as with the intermediate settlements. In the southwestern part of the area, it seems to cross a part of the national highway and in the eastern part, near the lake, there is a military airport. Cracking on the housing, building and streets are examples of infrastructures problem due to the land subsidence. The subsidence it also badly influences the quality of the living environment and life

(e.g. health and sanitation condition) in the affected areas (Andreas *et al.* 2018). The economic losses caused by land subsidence are also crucial. All the above infrastructures are exposed to the natural hazard of the subsidence and show the importance of this study. As we will see in the results chapter, high speeds of average annual subsidence are recorded in the center of the plain, affecting a part of the railway and main road network of the area as well as the settlements located in it.

2.4 Physical Geography - Geology

Thessaly is dominated by a vast plain, the largest in Greece. The geomorphology of Thessaly is controlled by two orientations of normal faults. The main NW-SE trending basins of Karditsa and Larissa and their separating range are controlled by NW-SE trending normal faults (Caputo and Pavlides 1993). The study area of this master thesis is the eastern part of the Southern Thessaly plain which is characterized as perfect, almost, elongated plain at the foot of Ossa and Montenegro with a length of 35 km. Its height ranges from 46 to 48 m. and the only territorial irregularities are a series of small swamps. During of the Pleistocene and the Holocast, it is possible that the fine alluvium was deposited in the farthest area of the deposited cones at the foot of the eastern mountain range after the torrents that groove the slopes of the central hills and which have covered the terrestrial anomalies created by tectonic movements. The plain is bounded to the east by fault-controlled flanks of coastal ranges, more than 1,000 m high, in the SE continuation of Olympus Mt. All these ranges originate from rapidly exhumed and uplifting mantle rocks (Kontogianni *et al.* 2007).

Eastern Thessaly plain represents a tectonic depression of Quaternary age, corresponds to a gently SE- dipping, nearly planar surface covered by a thick (up to 50 m deep) alluvium layer, relict of a Quaternary Lake, which was gradually restricted to the Karla Lake, at its lowest, SE part. Basement rocks are found at a depth of 50–250 m, although some deeper, probably tectonic depressions with the basement at a depth of 500–700 m, have been noticed. In some parts, however, basement rocks crop out slightly above the ground surface. Quaternary sediments overlay basement rocks, mostly carbonate rocks and schists, except for a narrow strip of Neogene sediments along the western margin of the plain. Very rich aquifers are observed in the poorly consolidated Quaternary formations and in the karstified carbonate rocks of the

basin bedrock. The depth of water table varies considerably within the area. The bedrock geology consists of gneiss, schists, marbles, quartzites, serpentinites, flysch, and carbonate formations (Figure 4).

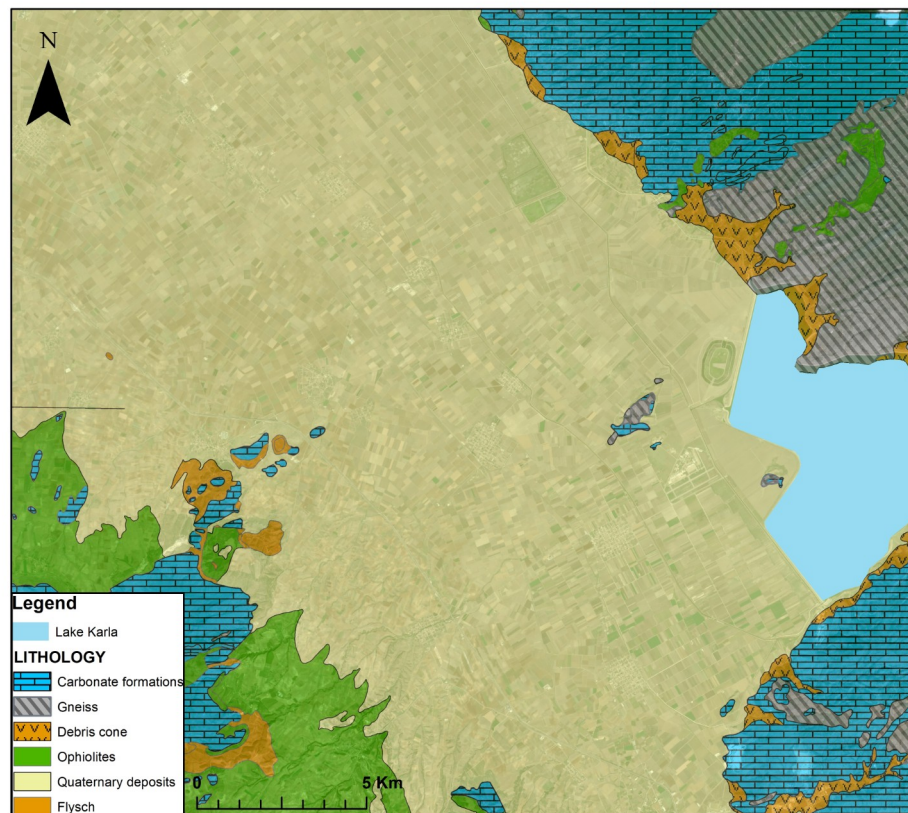


Figure 4: Geological map of the eastern plain of Thessaly, source: Institute of Geology and Mineral Exploration (IGME). Contains modified Sentinel-2 Copernicus data as basemap.

Eastern Thessaly belongs to the Internal Hellenides which are part of the Greek orogenic belt. The build up of the whole mountain chain is the result of several compressional events. The last of these events was the Alpine tectonic phase (e.g. Aubouin, 1959), which affected Thessaly from Eocene to Middle Miocene times (Brunn, 1956). After the Alpine orogenesis, Eastern Thessaly, underwent extensional tectonic conditions. Probably related to the post-orogenic collapse (Caputo & Pavlides, 1993), the area was affected by a NE-SW extensional regime. This caused the formation of a system of NW-SE elongated horsts and grabens bounded by large normal faults. As a consequence of this event, the structural trend of the Hellenides, as inherited from the Alpine orogenesis, was emphasised. In Thessaly, this tectonic regime was active from Pliocene, or possibly from Latest Miocene, to Lower Pleistocene times (Caputo,

1990). In Figure 5, are shown the major faults active during this deformational event. Large positive and negative signs show the vertical movements affecting the major fault-bounded blocks.

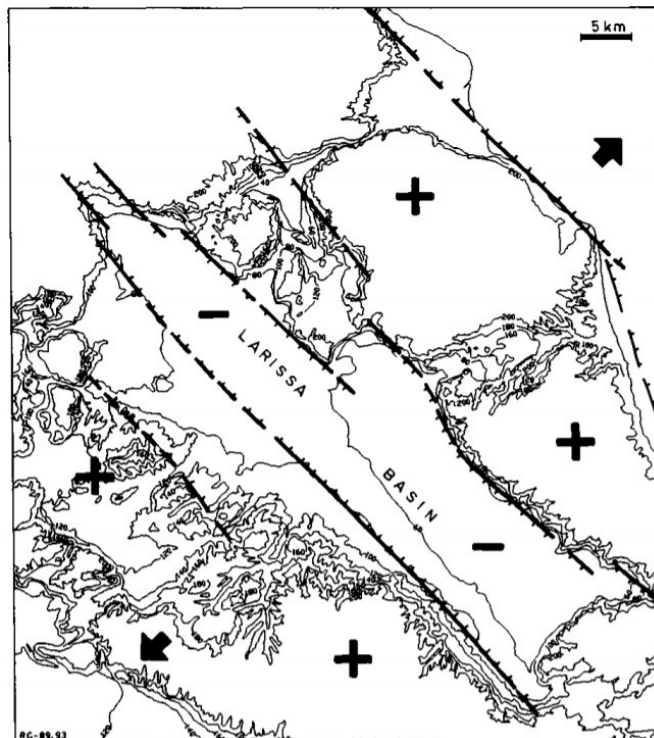


Figure 5: Simplified structural map of eastern Thessaly showing the major normal faults activated during the Pliocene-Lower Pleistocene extensional régime which generated the NW-SE trending Larissa Basin (Caputo *et al.*1994)

From a structural point of view, the importance of this tectonic phase is to generate the NW-SE trending Larissa Basin that still dominates the morphology of this area. The present Larissa Plain more or less coincides with this major tectonic structure.

After a period of geodynamic stability, a new tectonic regime affects the area. It is extensional as the former one but characterised by a N-S to NNE-SSW stretching direction (Caputo, 1990). This tectonic phase started during Middle-Late Pleistocene and is still active nowadays as inferred from the recent and historical seismic activity in the broader region. This tectonic phase is very important for the structural evolution of Thessaly and particularly of the northern Larissa Plain. According to the new geodynamic conditions affecting the area, a new System of normal faults, mainly trending E-W to ESE-WNW, forms. Although, most of these faults across or ignore

the older NW-SE trending ones, it is obvious that the latter played an important role during the nucleation of the new structures. Nonetheless, some of the Pliocene normal faults were reactivated but with an oblique sense of movement (Caputo, 1992).

It is less active seismically in modern and historical times with four large earthquakes occurred, in 1954 (M=7.0; Palyvos *et al.* 2010), in 1955 (M=6.2; Ambraseys and Jackson 1990), in 1957 (M=6.8; Papazachos *et al.* 2016) and in 1980 (M=6.5; Papazachos *et al.* 1983). An M=6.1 shallow event occurred near Larisa in 1941 (Galanopoulos, 1950; Ambraseys & Jackson, 1990) located the epicenter several kilometers NNE from Larissa causing extensive damage to settlements in wide area.

Groundwater pumping

Since the draining of the Karla Lake in 1962 and land redistribution for agricultural activities, water demands were increased. As surface water could not cover such needs, a big number of drill holes were bored in the plain (Gouvi, 2003) causing an over-exploitation of the groundwater and finally leading to progressive decline of the aquifer head and a continuous need for opening deeper drillings to exploit deeper aquifers. It is estimated that between 1978 and 2003 ta significant drop of the underground water level between 10 and 50 m (Figure 6), with a maximum of 100 m (Kontogianni *et al.* 2007).

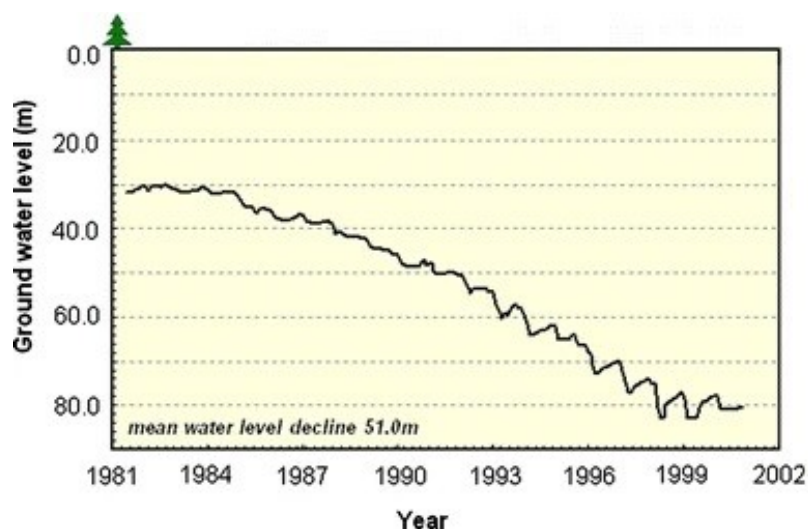


Figure 6: Graph of groundwater withdrawal versus time at a borehole at Niki village area. Mean water level drop measured from the ground surface is about 51 m in 20 years (1981–2001) (Kontogianni *et al.* 2007)

According to investigation of Polyzos *et al.* (2006) in five boreholes over 25 years shows a stability in groundwater levels for the first five years (1980-1985). Between 1985 and 2000 the aquifer level following a continuous drop despite the fact that the rainfall for this period was relative intense. In Figure 7 showing a drop of 45 – 50 m for Niki and Kipseli (Kileler) settlements.

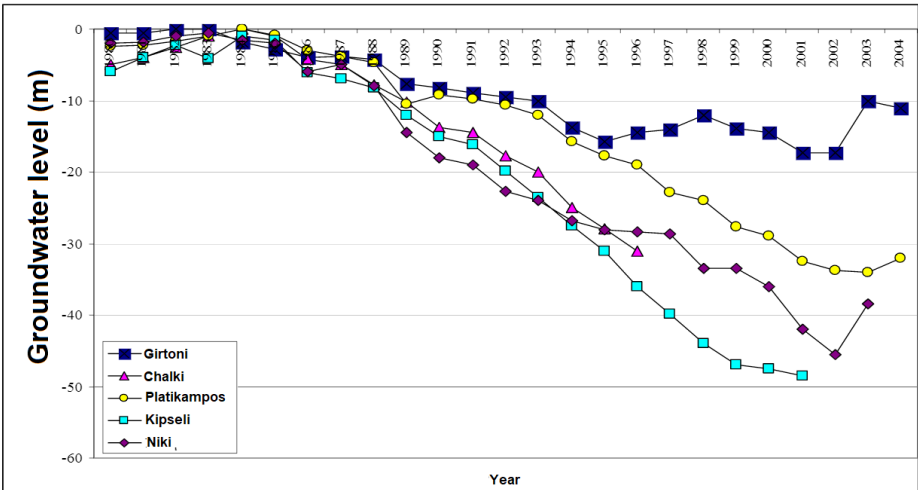


Figure 7: Graph of groundwater withdrawal versus time at a borehole at five settlements of Girtoni, Chalki, Platiampos, Kipseli(Kileler) and Niki for time period of 1985-2004. Modified Polyzos *et al.* 2006

2.5 Climate of Larissa Plain

Larissa Plain has continental climate which is characterized by constant fluctuations on her mean monthly temperatures across the years with the higher values detected on August up to 27 C and the lower on January up to 3 – 5 C. Average annual temperature and precipitation is about 16 to 17 °C and 500-600 mm respectively. The warmest months is July and August and the coldest is January, the February and December. Frosts occur in November - April and relatively often. The amount of precipitation is relatively high in Winter months from October to January, while the most dry are July and August.

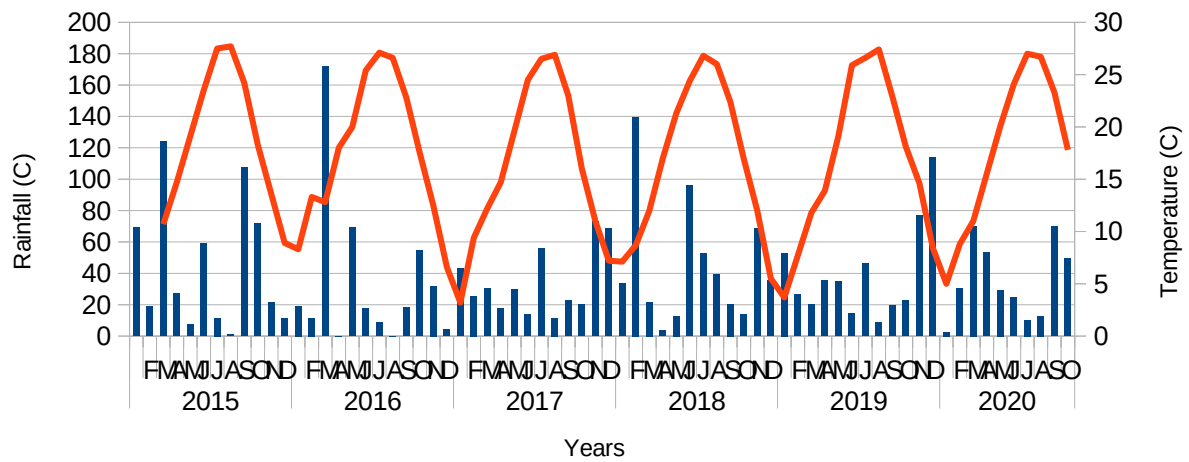


Figure 8: Meteorological Data of Larissa Plain 2015-2020. Blue bars representing rainfall and red lines the mean temperature of every month.

Meteorological data of rainfall and average heat collected from two local weather stations of the National Observatory of Athens during 2015-2020. For the period of 2015-2017 were used a meteo station located in city of Volos 25 km SE far from the study area (39.36076°N,22.93165°E) and a second for the period of 2017-2020 located in Halki 16 Km NW far from the study area (39.57083°N, 22.54333°E).

3. Climate Change

Climate change is a change that is detected in the motive of weather and related changes in oceans, land surfaces and ice sheets, occurring over time scales of decades(Nasa). Climate change describes a change in the average conditions — such as temperature and rainfall — in a region over a long period of time. Earth's climate has constantly been changing — even long before human appearance. However, scientists have observed unusual changes recently on Earth's average temperature which has been increasing much more quickly than they would expect over the past 150 years. As Earth's climate continues to warm, the intensity and amount of rainfall during storms and the heat waves appearances are e expected to increase

There are lots of factors that contribute to Earth's climate. However, scientists agree that Earth has been getting warmer in the past 50 to 100 years due to human activities. Scientists attribute the global warming trend observed since the mid-20th century to the human expansion of the "greenhouse effect"— warming that results when the atmosphere traps heat radiating from Earth toward space.

The greenhouse effect is a process that occurs when gases in Earth's atmosphere trap the Sun's heat. This process makes Earth much warmer than it would be without an atmosphere. The greenhouse effect is one of the things that makes Earth a comfortable place to live. The gases that contribute to the greenhouse effect are referd as greenhouse gases and include Water vapors, Carbon dioxide (CO₂), Methane, Nitrous oxide and Chlorofluorocarbons.

Human activities are changing the natural greenhouse. Over the last century the burning of fossil fuels like coal and oil has increased the concentration of atmospheric carbon dioxide (CO₂). This happens because the coal or oil burning process combines carbon with oxygen in the air to make CO₂. To a lesser extent, the clearing of land for agriculture, industry, and other human activities has increased concentrations of greenhouse gases.

According to NASA the consequences of changing the natural atmospheric greenhouse are difficult to predict, but some effects seem likely:

- On average, Earth will become warmer. Some regions may welcome warmer temperatures, but others may not.
- Warmer conditions will probably lead to more evaporation and precipitation overall, but individual regions will vary, some becoming wetter and others dryer.
- A stronger greenhouse effect will warm the ocean and partially melt glaciers and ice sheets, increasing sea level. Ocean water also will expand if it warms, contributing further to sea level rise.

Climate change and land subsidence

Climate change will further magnify the risks such as soil movements will become more frequent and severe. Rising average temperatures, combined with Increased variability in precipitation and more extreme weather events can lead to longer periods of droughts and floods . In long periods of droughts there is a higher risk of depletion of aquifers, especially in case of small and shallow aquifers. People in water-scarce areas will increasingly depend on groundwater, because of its buffer capacity. A long and intense dry spell can increase the demand of groundwater for human activities and land use, can lower the ground so much that it creates fissures in the earth and tears apart the foundations of houses, bridges, industrial sites and other structures. As the trend towards drier weather continues, occurrences of drought and soil subsidence will become even more frequent and more severe (IGRAC, Reichenmiller, 2011).

Climate change in Greece

As the climate change is a global scale phenomenon, group of scientist (Giannakopoulos *et al.* 2011) carried out investigations for potential implications over Greece. The most relevant results to our study area are realated with:

- In many of the agricultural areas, an increase in precipitation is projected. More specifically, the areas of Larissa and southern Evia will experience increases of up to 20%
- The largest changes seem to occur in the cities of Thessaloniki, Patras, Kalamata, Larissa and Lamia where more than 20 hot days per year are expected.
- The total annual precipitation is found to decrease in Lamia, Larissa, Volos, Thessaloniki and Athens.
- Dry days is expected to increase in most of the studied agricultural regions.

4. Literature Review

A great number of researchers demonstrated the InSAR methods to detect and measure ground subsidence, caused by the removal of subsurface groundwater. There are numerous studies that apply the SBAS algorithm for land subsidence and some specific studies which observe the southern basin of Thessaly with different methods and techniques. Some of the papers that are most relevant to our study are presented below.

Parcharidis *et al.* (2011) applied a DInSAR technique in Larissa Plain to measure ground deformation despite the unfavorable conditions inducing decorrelation. For the purpose of their study, have been used 48 ERS-1 and ERS-2 SAR scenes and 39 ENVISAT ASAR scenes. By exploiting differential interferometric pairs of short temporal separation and perpendicular baselines, it was possible to identify the area affected by ground deformation. Seasonal deformation signals were recognized at the southwestern part of the basin, reaching several centimeters during the summer period. The area of maximum deformation is located in Kileler village, reaching -17.5 cm along the line of sight in the summer of 1998. During winter seasons deformation is considerably reduced to -0.5 cm and -0.1 cm.

Benekos *et al.* (2014) focuses to quantitatively measured deformation over the plain of south Thessaly since it is an area that undergone excessive water pumping and led to significant subsidence the past 20 years. Scenes from two different datasets and two different satellites were utilised in order to investigate the study area. Advanced SAR (ASAR) scenes from Envisat satellite in Descending orbit and 14 scenes from ALOS-PALSAR satellite in both single and dual polarization and Ascending orbit as well, covering a total time span of 7 years (2003-2010) for Envisat ones and 4 years (2007-2011) for ALOS-PALSAR were used, respectively. method that was primarily selected to reveal the deformation patterns in the area and the evolution of it in the temporal dimension was PSI (Persistent Scatterers Interferometry). The results shows high subsidence rates in some villages with a notable subsidence pattern at the center of the plain following possibly the basin of the area. Due to the high and rapid rates of deformation in the area, IPTA failed to deliver sufficient and accurate results. Since PSI technique was ruled out, a “hybrid INSAR” methodology using elements of conventional DInSAR, short baseline interferometry approaches.

Foumelis *et al.* (2016) have applied Persistent Scatterers (PS) and Small Baselines (SB) interferometric techniques to study the history of ground deformation along the entire Larissa plain using Environmental Satellite (ENVISAT) advanced synthetic aperture radar (ASAR) data (IM mode in IS2 swath), comprising 30 scenes acquired in descending track 279, covering the period from 2002 to 2010. Their findings outline the southern part of the basin as the mostly affected area, whereas local subsidence patterns of lower magnitude were also recognized elsewhere. Although average ground deformation rates do not exceed 2 cm year⁻¹, line-of-sight (LOS) displacements of up to 13 cm were observed, occurring during the summer–autumn periods.

Fylaktos *et al.* (2019) have applied Persistent Scatterers (PS) interferometric technique to investigate the ground deformation in the southern part of Larissa plain using 89 SAR scenes of Sentinel 1 A & B SLC IW covering the period 2014-2018. Moreover they have used optical data from Landsat program and Copernicus Sentinel 2 to monitor the evolution of water recharge of the new lake as well as seasonal changes in the level for one year and compare with the corresponding annual interferometric results. According to their findings, Karla reservoir is refilled but the subsidence rates remains the same compared to past research from 1993 to 2010 and seasonal subsidence meaning a partial natural recharge of ground water in the area.

Hu *et al.* (2019) in their study they apply the SBAS-InSAR technique to monitor the land subsidence in Fuzhou downtown after the program of metro construction. 24 scenes of X-band TerraSAR data from July 2013 to August 2015 and 32 scenes of C-band Sentinel-1 data from July 2015 to February 2018 were used in this experiment. Their results show a maximum subsidence rate of -12mm/yr, and eight subsidence funnels have been found during the observed period. After analyzing the subsidence of these regions in a long time span, it can be concluded that there are three regions that have a relatively stable disastrous subsidence effect, and there is a possibility of further intensified subsidence.

Another research by Hu *et al.* (2019) focuses on the land subsidence phenomenon using InSAR and Global Navigation Satellite System (GNSS) technology. They applied two different kinds of time-series InSAR (TS-InSAR) methods: Small Baseline Subset (SBAS) and the Permanent Scatterer InSAR (PSI) process on a dataset with 31 Sentinel-1A Synthetic Aperture Radar (SAR) images. From their processing, they have generate the surface deformation field of Shenzhen, China and Hong Kong Special Administrative Region (HKSAR). The time series of the 3d variation of the reference station network located in the HKSAR was generated at the same time. They compare the characteristics and advantages of PSI, SBAS, and GNSS in the study area. They mainly focus on the variety along the coastline area. From the results generated by SBAS and PSI techniques, discovered the occurrence of significant subsidence phenomenon in the land reclamation area, especially in the metro construction area and the buildings with a shallow foundation located in the land reclamation area.

Argyris *et al.* (2020) were combined for almost 10 years of continuous GNSS observations at four permanent stations with groundwater and rainfall data to investigate subsidence patterns in the region of Thessaly, central Greece. Through their study, they came to the conclusion that anthropogenic subsidence continues at southeast Thessaly (Karla reservoir region) up to autumn of 2017 because the vertical time-series data of the only one station in the southern Larissa plain of STEF (Stefanovikio), reach a cumulative value of 55 cm and show a “rampfat” pattern that correlates with neighboring borehole data. The GNSS stations in Karditsa (KRDI) and Larissa (LARM) show a correlation with groundwater-level fluctuations but no subsidence. Station KLOK (Klokotos) shows a small subsiding trend (-0.38 mm/yr) with no correlation to either groundwater levels or to rainfall patterns; therefore, its seasonal periodicity may reflect geodynamic (plate) motions.

Cigna *et al.* (2020) observe the metropolitan area of Mexico City which is one of the fastest sinking cities globally. For the purposes of their study, they used more than 300 Sentinel-1 Synthetic Aperture Radar Interferometric Wide swath mode scenes acquired in 2014–2020. Their methodology is based on two-pass differential Interferometric SAR (InSAR) and the parallelized Small Baseline Subset (SBAS) repeat-pass InSAR in order to provide a complete account of spatial patterns, long-term trend and present-day settlement rates affecting the city. The 3D deformation field reveals that foremost is the role of the vertical velocity VU, with peaks

around -32.0 and -39.1 cm/year. East-west rates are limited, except for some horizontal strain (up to ± 5 cm/year) within the subsidence bowls. Moreover, the results that have been produced from the 2014–2019 InSAR time series, were compared with 2008–2020 GPS data.

Kamila Pawluszek-Filipiak *et al.* (2020) uses radar interferometry to analyze the mobility of an urban and suburban area of Greater Tunis region. The small baseline subset (SBAS) method was applied in order to monitor the spatial and temporal pattern of the deformation phenomena in the study area. The analysis based on Envisat ASAR (2003–2007, descending satellite orbit) and Sentinel 1B (2016–2018, ascending satellite orbit) SAR data in order to create deformation velocity maps associated with the line of sight displacement time series. The results obtained by this method showed the existence of subsidence phenomenon in the urban areas (Tunis City) as well as in the rural areas (Mornag plain). In the first site (Tunis City), the subsidence rate reaches up to 13.98 mm/year and 19 mm/year during 2003–2007 and 2016–2018, respectively. The ground deformation that is detected around the region of Tunis Lake and Sebkheth Essijoumi, is probably due to the nature of the highly compressible and thickness alluvial deposits and whose substratum depth sometimes reaches more than 60 m. In the second studied site, ground subsidence was identified in the whole plain of Mornag. Indeed, the comparison between piezometric data and time series deformations shows that the trend of soil subsidence is coherent with the dynamic change in groundwater levels. Furthermore, the analysis of velocity deformation, geological data and hydrogeological information allows us to associate all the detected settlement patterns to groundwater overexploitation and compressible alluvium all over the plain. This overexploitation of groundwater in Mornag plain is mainly caused by the expansion of agricultural and industrial activities and the decrease in annual rainfall in recent years (from 2003 to 2018).

5. Basic Principles

Remote sensing, also called earth observation, refers to obtaining information about objects or areas at the Earth's surface without being in direct contact with the object or area. Remote sensing techniques allow taking images of the earth surface in various wavelength region of the electromagnetic spectrum (EMS). One of the major characteristics of a remotely sensed image is the wavelength region it represents in the EMS. There are two basic satellite systems for monitoring and imaging the Earth:

1. Remote sensing systems that record "natural" radiation are called passive. For reflected energy this happens during the day when the sun illuminates parts of it Earth, while there is no reflected energy at night. Naturally emitted energy (thermal infrared) can be recorded day or night and if the amount of energy is such that it is recording possible.

2. Active systems are those that record electromagnetic waves that transmitted from another external source or from the recorder itself. Usually the recording system is what emits energy to the surface and then is reflected back and forth the "echo" of the signal from the system itself is recorded. A typical example of this type instrument are the Radars that emit in the microwave area. On this master thesis, we will focus only in active systems (Parcharidis, 2011).

5.1 Radar

Radar is the abbreviation for the English expression Radio detection and ranging, which indicates that the system operates in the spectral bands of radio waves and microwaves and detects the reflected or radiated energy from the ground (Mertikas, 2009). Radar called active systems because their ability to emit microwave radiation at a specific frequency from an antenna located on the satellite or the aircraft, to the earth's surface and record the back-scattered radiation. Microwave radiation passes through the atmosphere to the earth's surface, is scattered or reflected, and then a part of it returns to the satellite antenna, while the rest is lost in a different direction (Parcharidis, 2016). The recording the time that takes to return of the pulse in the satellite instruments is what determines the place of earth features on the image. The Radar signal is emitted to the right of the satellite's motion and strikes at an angle to the earth's surface. The objects on the ground reflect the micro-radiation according to their geometric and dielectric characteristics and the Radar receiver records the back-scatter signal (echo) (Kartalis and Feidas 2013). Apart from the fact that Radar is an active system, it differs

from other Remote Sensing methods because the data is recorded based on the time of passage and return of radiation, and not the angular distance, as cameras and optical scanners do (Mertikas, 2009). There are two types of Radar imaging used in Remote Sensing: Real Aperture Radar (RAR) and Synthetic Aperture Radar (SAR) (ESA).

Understanding imaging radar remote sensing is more difficult than visual means because technology is more complex and the data recorded are more varied. Optical technology works at wavelengths of about $1\mu\text{m}$, while radar systems at wavelengths of a few centimeters. From this difference, the characteristics of the Earth's surface appear differently on radar than in optics sensors. Moreover, radar system enable to detect features and data which the visual spectrum are impossible to detect. This feature is also a result of penetration that can be achieved by systems operating in its microwave section electromagnetic spectrum due to the long wavelength. In many cases, taking always take into account other factors such as the humidity, the longer the wavelength the greater the ability to penetrate. Radar systems provides the control over the properties of incident energy. This allows us to have a variety of data types to be recorded, and innovative applications such as topographic surveying, landscape change detection and, to a limited extent, 3D modeling of the volume detail of an element.

Radar sensors utilize longer wavelengths at the centimeter to meter scale, which gives it special properties, such as the ability to see through clouds(100 GHz -300 MHz). The different wavelengths of SAR are often referred to as bands. The names of the various spectral zones were derived from military encryptions used during World War II, and the identification of the names was completely random and arbitrary with letter designations such as X, C, L, and P.

Frequency band	Frequency range (GHz)	Wavelength range (cm)
L band	1–2	15–30
S band	2–4	7.5–15
C band	4–8	3.75–7.5
X band	8–12	2.5–3.75
Ku band	12–18	1.67–2.5
K band	18–27	1.11–1.67
Ka band	27–40	0.75–1.11
V band	40–75	0.4–0.75
W band	75–110	0.27–0.4

Table 1: Table showing the frequency and wavelength of every band in microwave spectrum.

Microwave recording systems are called all-weather, as they have the advantage of operating independently of sunlight, and therefore have the ability to operate during the day and night, and are generally not sensitive to adverse weather conditions, weather and cloud cover. This results in minimal or no attenuation of microwave radiation as it passes through the atmosphere (Drury, 1987). Atmospheric absorption and scattering are minimal at most microwave wavelengths. The ability of microwave radiation to penetrate rainfall and below the earth's surface increases with wavelength. Thus long-wave microwaves such as L- (15-30cm) and P-waves (30-100cm), are not affected by clouds and rainfall and have the ability to penetrate dry surfaces such as sand, snow and vegetation. , in depth (Mertikas, 2009).

5.2 SAR Satellites

Synthetic Aperture Radar, or SAR, is a complex Radar system. It has day and night operational and cloud-penetrating capabilities because it is an active system using microwaves. The SAR antenna has its long axis in the flight direction also called the azimuth direction and the short axis in the range direction. The basic function of the Radar includes the transmission of a minimum time (microsecond) high signal energy and the recording of recreation from the earth surface of this signal. The information recorded is directly related with the relative strength of the signal, the time between the transmitted and incoming signal, and the address from which the reflected signal comes from. The radar sends pulses to one side of the ground track that illuminates the earth over a large elliptical footprint. The reflected energy returns to the radar where it is recorded as a function of fast time in the range direction and slow time, or echo number, in the azimuth direction. A radar image is a matrix of complex numbers. The focused image contains both amplitude (backscatter) and phase (range) information for each pixel. Amplitude values represent the radar backscatter and visualized with a gray scale. The brighter the pixel, the stronger the backscatter. The phase value is related to the sensor-to-target distance and the interaction of the e.m. singal with the radar target (Ferretti, 2014).

5.2.1 SAR Acquisition Geometry

SAR satellites collect swaths of side-looking echoes at a sufficiently high range resolution and along-track sampling rate. As discussed in this appendix, the range resolution of the raw radar data is determined by the pulse length and the incidence angle. Satellite sensors are mounted on their platforms with the direction of transmission orthogonal to that flight direction. The earlier satellites were all right looking satellites, meaning that the microwave beam was transmitted and received on the right side only of the satellite, relative to its orbital path. More recent satellites have both right looking and left looking capabilities (although the default mode is usually right looking), thus they can look to the right or to the left of the craft, but not both directions simultaneously. Most satellites look angle is between 20-50 degrees. It should be noted that due to the Earth's curvature, the incidence angle of the radiation on a flat horizontal terrain is larger than the off-nadir angle. The direction alongside the sensor Line of Sight (LOS) is defined as the slant-range direction. The off-nadir angle is always nonzero, since the radar would receive the echoes from the detected targets at nearly the same time, making possible to create an image. The antenna receives radar echoes while moving at a few km/sec and so it is in different locations compare to where it had transmitted each pulse.

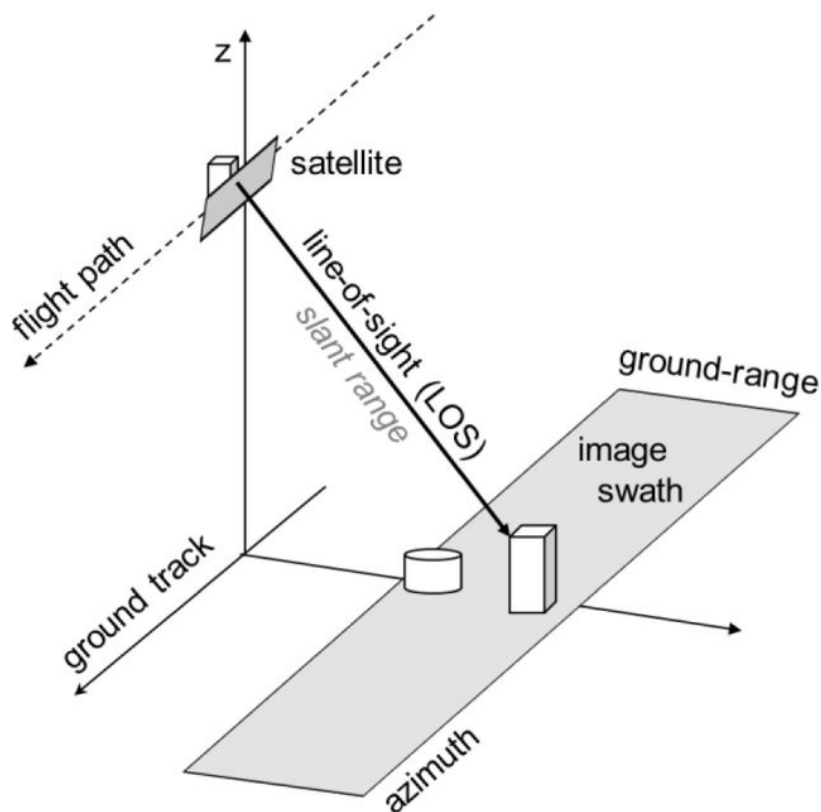


Figure 9: SAR geometry acquisition (Henschel *et. al*, 2016).

5.2.3 Interaction of SAR signal with the earth's surface

SAR systems measure the amplitude of the radiation backscattered from surface objects (scatterers) and specify the digital number for each pixel. The amplitude depends on many factors including observation parameters (wavelength, frequency, polarization, incident angle of the emitted wave) and surface parameters (embossing-roughness, geometric shape and dielectric properties of objects). Moreover, depending on the wavelength, radiation penetrates the surface material at various depths. Figure 10 shows the different deep penetration of zones X, C and L, which increases with wavelength and absence of humidity. The relief of the earth's surface plays an important role. Targets with high backscattered signal are identified as bright spots in the radar images and flat smooth surfaces are represented as dark areas, since the radiation is reflected away from the radar. Amplitude images are displayed by means of grey scale levels.

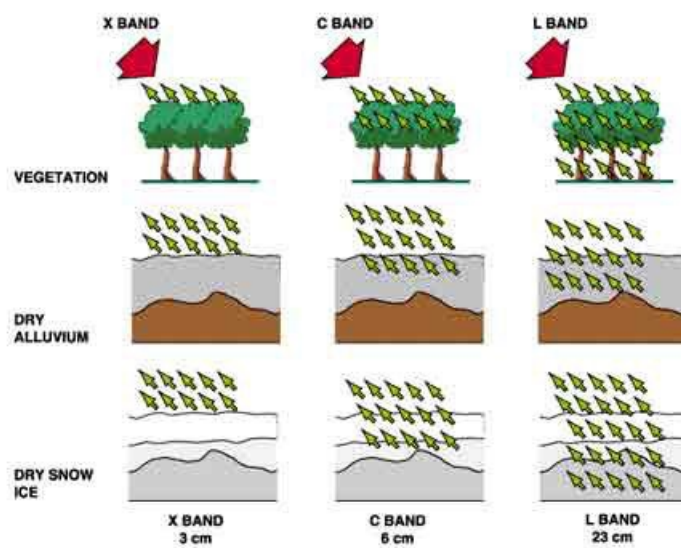


Figure 10: : X, C & L bands penetration (ESA)

5.2.4 SAR Characteristics

SAR systems can synthesize a virtual antenna much longer than real radar, taking advantage of platform movement and doppler effect using special back-recording signal processing and processing procedures. For example an antenna of 10 m it is possible to simulate a virtual antenna of 600 m (Mertikas, 2009). The spatial resolution of radar data is directly related to the ratio of the sensor wavelength to the length of the sensor's antenna. For a given wavelength, the longer the antenna, the higher the spatial resolution (Earthdata).The length of the antenna is subject to technicians restrictions and ranges from 1-2m on airborne platforms and from 10-15m on satellites.

Radar can also collect signals in different polarizations, by controlling the analyzed polarization in both the transmit and receive paths. Polarization refers to the orientation of the plane in which the transmitted electromagnetic wave oscillates. While the orientation can occur at any angle, SAR sensors typically transmit linearly polarized. The horizontal polarization is indicated by the letter H, and the vertical polarization is indicated by V. The advantage of radar sensors is that signal polarization can be precisely controlled on both transmit and receive. Signals emitted in vertical (V) and received in horizontal (H) polarization would be indicated by a VH. Alternatively, a signal that was emitted in horizontal (H) and received in horizontal (H) would be indicated by HH, and so on.

SAR system is a coherent sensor. Speckle noise or "Salt & Pepper" is a phenomenon in all coherent imaging systems. The source of this noise is attributed to random interference between the coherent returns, issued from the numerous scatterers present on a surface, on the scale of a wavelength of the incident radar wave. The presence of speckle may decrease the utility of SAR imagery by reducing the ability to detect ground targets and obscuring the recognition of spatial patterns (Sheng and Xia, 1996). Noise can be reduced without being able to eliminate it completely, with various processing techniques, since the image has already been reduced by the multi-looking technique, before it is acquired by the user. The use of special filters can reduce noise and, depending on their size (3x3, 5x5, etc.), the homogenization of primary data it can be small or large

It should be mentioned that geometric distortions associated to a regular sampling in range.

The geometrical distortions are:

- Shading: This phenomenon is observed on steep slopes that are not visible on the satellite and having an opposite aspect (Parcharidis, 2011).
- Foreshortening: Slopes that face the radar sensor, affected by “foreshortening” and the backscatter signal corresponds to very bright pixels. This is caused because the resolution cell can be hundreds of meters in ground range and more power can be backscattered towards the radar sensor, compared to flat terrain.
- Layover: It is an extreme case of foreshortening. When the radar beam reaches the top of a mountain or a tall feature before it reaches the base. The return signal from the top is received by the sensor before the signal from the bottom. This effect occurs whenever the local slope exceeds the off-nadir angle, therefore as with foreshortening, layover is most severe of radar acquisitions at small off-nadir angles (Ferretti, 2014).

Terrain deformations can be corrected using a digital elevation model (DEM). On the other hand, hiding information due to shading or foreshortening and layover is not easy to replace. Partial replacement can be achieved, using a second acquisition of opposite orbit.

One of SAR's advantages is it can detect the Earth's surface by two different acquisition geometries-modes, the descending and the ascending. All satellites equipped with SAR sensors have a near-polar orbit according to Earth's relative orbit, while their angle is in the range of ten degrees. By combining Earth's rotation and satellite's orbital paths, the entire Earth's surface can be illuminated by two different satellite geometries. The satellite in descending mode, travels from the north to south it views a target location looking westward (in right-looking mode), while the ascending mode moves from the south to north, it views the same target eastward (Ferretti, 2014).

5.3 Copernicus Programme

Copernicus is the European system for monitoring the Earth and is coordinated and managed by the European Commission.

The development of the observation infrastructure is performed under the aegis of the European Space Agency for the space component and by the European Environment Agency and EU countries for the in situ component. It consists of a complex set of systems which collect data from multiple sources: earth observation satellites and in situ sensors such as ground stations, airborne sensors, and sea-borne sensors. It processes this data and provides users with reliable and up-to-date information through a set of services related to environmental and security issues.

The services address six thematic areas: land, marine, atmosphere, climate change, emergency management, and security. They support a wide range of applications, including environment protection, management of urban areas, regional and local planning, agriculture, forestry, fisheries, health, transport, climate change, sustainable development, civil protection, and tourism(European Commission).

5.4 Satellites systems

5.4.1 Copernicus program-Sentinel 1 constellation

The SENTINEL-1 mission is the European Radar Observatory for the Copernicus joint initiative of the European Commission (EC) and the European Space Agency (ESA). SENTINEL-1 is designed to work in a pre-programmed, conflict-free operation mode, imaging all global landmasses, coastal zones and shipping routes at high resolution and covering the global ocean with vignettes. This ensures the reliability of service required by operational services and a consistent long-term data archive built for applications based on long time series.

The mission is composed of a constellation of two satellites, SENTINEL-1A and SENTINEL-1B, sharing the same orbital plane with a 180° orbital phasing difference, and together achieve very short revisit times(6 days) and rapid product delivery. The Sentinel-1A was launched on 3 April 2014 and Sentinel-1B on 25 April 2016. Synthetic Aperture Radar (SAR) has the advantage of operating at wavelengths not impeded by cloud cover or a lack of illumination and can acquire data over a site during day or night time under all weather conditions. The SENTINEL-1 mission includes C-band SAR imaging ($f = 5.405$ GHz, $\lambda = 5.547$ cm) with its C-SAR instrument, which can offer reliable, repeated wide-area monitoring. The C-SAR instrument supports operation in dual polarisation (HH+HV, VV+VH) implemented through one transmit chain (switchable to H or V) and two parallel receive chains for H and V polarisation. Dual polarisation data is useful for land cover classification and sea-ice applications(ESA).



Figure 11: Sentinel-1 spacecraft (ESA, 2012)

SENTINEL-1 operates in four exclusive imaging modes with different resolution (down to 5 m) and coverage (up to 400 km):

- **Stripmap (SM)** 5 m by 5 m resolution over a narrow swath width of 80 km
- **Interferometric Wide swath (IW)** mode allows combining a large swath width (250 km) with a moderate geometric resolution (5 m by 20 m).
- **Extra-Wide swath (EW)** works similarly to the IW mode employing a TOPSAR technique using five sub-swaths instead of three, resulting in a lower resolution (20 m by 40 m)
- **Wave mode (WV)**. composed of stripmap imageries of 20 km by 20 km, acquired alternately on two different incidence angles. Wave imageries are acquired every 100 km, with imageries on the same incidence angle separated by 200 km.

Sentinel-1 can provide the following product types of data:

Level-0

The SAR Level-0 products consist of the sequence of Flexible Dynamic Block Adaptive Quantization (FDBAQ) compressed unfocused SAR raw data. For the data to be usable, it will need to be decompressed and processed using a SAR processor.

Level-1

Level-1 data are the generally available products intended for most data users. Level-1 products are produced as Single Look Complex (SLC) and Ground Range Detected (GRD).

Single Look Complex (SLC) products consist of focused SAR data geo-referenced using orbit and attitude data from the satellite and provided in zero-Doppler slant-range geometry. The products include a single look in each dimension using the full transmit signal bandwidth and consist of complex samples preserving the phase information.

Ground Range Detected (GRD) products consist of focused SAR data that has been detected, multi-looked and projected to ground range using an Earth ellipsoid model. Phase information is lost. The resulting product has approximately square spatial resolution pixels and square pixel spacing with reduced speckle at the cost of worse spatial resolution.

GRD products can be in one of three resolutions:

- Full Resolution (FR)

- High Resolution (HR)
- Medium Resolution (MR).

The resolution is dependent upon the amount of multi-looking performed. Level-1 GRD products are available in MR and HR for IW and EW modes, MR for WV mode and MR, HR and FR for SM mode.

Level-2

Level-2 OCN products include components for Ocean Swell spectra (OSW) providing continuity with ERS and ASAR WV and two new components: Ocean Wind Fields (OWI) and Surface Radial Velocities (RVL). The OSW is a two-dimensional ocean surface swell spectrum and includes an estimate of the wind speed and direction per swell spectrum. The OSW is generated from Stripmap and Wave modes only. For Stripmap mode, there are multiple spectra derived from internally generated Level-1 SLC images. For Wave mode, there is one spectrum per vignette. The OWI is a ground range gridded estimate of the surface wind speed and direction at 10 m above the surface derived from internally generated Level-1 GRD images of SM, IW or EW modes. The RVL is a ground range gridded difference between the measured Level-2 Doppler grid and the Level-1 calculated geometrical Doppler.

5.4.2 COSMO-SkyMed

COSMO-SkyMed (Constellation of Small Satellites for Mediterranean basin Observation) is a 4-spacecraft constellation, conceived by ASI (Agenzia Spaziale Italiana), and funded by the Italian Ministry of Research (MUR) and the Italian Ministry of Defense (MoD), Rome, Italy. Each of the four satellites is equipped with a SAR (Synthetic Aperture Radar) instrument and is capable of operating in all visibility conditions at high resolution and in real time. The overall objective of this program is global Earth observation and the relevant data exploitation for the needs of the military community as well as for the civil (institutional, commercial) community (ESA).

The constellation consists of 4 medium-size satellites, each one equipped with a microwave high-resolution synthetic aperture radar (SAR) operating in X-band, having ~600 km single side access ground area, orbiting in a sun-synchronous orbit at ~620km height over the Earth surface, with the capability to change attitude in order to acquire images at both right and left side of the satellite ground track (nominal acquisition is right looking mode). The Ground Segment is responsible for managing the constellation and granting ad-hoc services for collection, archiving and delivery of products to the users (ESA).

Mission	Launch date
COSMO-SkyMed-1	June 8, 2007 on a Delta-2 launch vehicle from VAFB, CA; Launch provider: ULA
COSMO-SkyMed-2	December 9, 2007 on a Delta-2 launch vehicle of ULA from VAFB, CA, USA
COSMO-SkyMed-3	October 25, 2008 on a Delta-2 launch vehicle of ULA from VAFB, CA, USA
COSMO-SkyMed-4	November 6, 2010 (UTC) on a Delta-2 launch vehicle of ULA from VAFB, CA, USA

Table 2: COSMO-SkyMed launch dates.

The program is managed in cooperation of ASI and MoD. Although the first generation constellation satellite SAR instruments (SAR-2000) will observe in X-band (9.6 GHz with a wavelength of 3.1 cm), multi-mode scenarios (X-, C- L- and P-band) are planned for the future.



Figure 12: Cosmo-skymed spacecraft

The mission imaging capability requirements call for very high peak power loads of up to 14 kW. The overall power consumption associated with a specific operating mode profile is:

	Spotlight	Stripmap	Stripmap	ScanSAR	ScanSAR
		HIMAGE	Ping Pong	Wide region	Huge region
Polarization	single	single	dual	single	single
Swath width [kmxkm]	10X10	40X40	30X30	100X100	200X200
Accessible swath	~620 km	~620 km	~620 km	~620 km	~620 km
Geometric Resolution [m]	1	3	15	30	100

Table 3: COSMO-SkyMed specific operating mode profile.

5.5 Interferometric Synthetic Aperture Radar

Interferometric Synthetic Aperture Radar (InSAR) is a technique for mapping ground deformation or estimating Digital Elevation Model (DEM), using radar images of the Earth's surface that are collected from orbiting satellites. The round trip distance from the satellite to the ground and back again is measured in units of the radar wavelength, and changes in that distance between the time two radar images were collected show up as a phase difference. Combining these two images is called "interfering" because combining two waves causes them to either reinforce or cancel one another. Attention must be paid to the sources of noise in InSAR analyses like atmospheric effect and phase decorrelation.

InSAR greatly extends the ability of scientists to monitor deformation phenomena (volcanoes, land subsidence, etc.) because, unlike other techniques that rely on measurements at a few points, InSAR produces a map of ground deformation that covers a very large spatial area with centimeter-scale accuracy (USGS).

The first interferometric results of earth-surface have shown up in 1986 from Zebker and Goldstein, who had used two airborne images of a region near San Francisco, California . They suggest that the radar interferometric measurements can be used to obtain high-resolution topographic maps of terrain believing that the interferometric technique is a new and useful approach to the remote determination of topographic data.

There are few image selection criteria concerning the two most important InSAR applications: Digital Elevation Model (DEM) generation and Differential Interferometry (DInSAR). The main parameters in order to get the best results from the SAR interferometric analysis are related with:

View angle (ascending and descending passes)

- Geometrical baseline
- Temporal baseline
- Time of the acquisition
- Coherence
- Meteorological conditions

Based on above the image selection must(ESA publications):

- Select either ascending or descending passes, depending on which will avoid foreshortening in the area of interest.
- Select those image pairs with the smallest perpendicular baseline in the required range of dates. The smaller the baseline, the smaller the topography contribution to the interferometric phase. As a consequence, a less precise DEM will be required for the topography subtraction. Moreover, the smaller the baseline, the higher the expected coherence.
- two interferometric SAR images are not simultaneous, the radiation travel path for each can be affected differently by the atmosphere. In particular, different atmospheric humidity, temperature and pressure between the two takes will have a visible consequence on the interferometric phase. The effect of such a contribution impacts on both altitude and terrain deformation measurements. Images with rainfall must be rejected.

Interferometric phase

The radiation transmitted by the radar sensors reaches the surface, is reflected and then returns to the radar sensor. This signal is sinusoidal and the delay (t) is equivalent to a phase change (ϕ) between transmitting and receiving the signal. Therefore the phase difference is equal to the bidirectional signal travel with distance 2R divided by the transmitted (λ) wavelength. The phase difference takes values from 0 to 2π (Parcharidis, 2011).

The phase values ϕ of a pixel P of a radar image can be modeled as a mixture of four different contributions (Ferretti, 2014):

$$\Phi (P)= \varphi + 4\pi/\lambda r + \alpha + \nu$$

where:

ϕ is the phase contribution due to the nature and location of all elementary scatterers within the resolution cell associated to pixel P coherently adding to form the radar return (referred sometimes and as the reflectivity phase),

$4\pi/\lambda r$ is the most important phase contribution for any InSAR analysis. Whenever there is a dominant scatterer within the resolution cell, r is the sensor-to-target distance.

α is a phase contribution, the free particles in the ionosphere and clouds, water vapour, rain, fog in the troposphere, affect the speed of propagation of the signal and introduce as a result effects on the phase detected by the receiving antenna (Hanssen, 2001). α is an important factor because most of the times is the greatest obstacle in conventional InSAR analyses and many times compromises the quality of the final results.

ν is related to any noise source, the most important is the thermal noise and it depends on the signal-to-noise ratio as it is related to the level of thermal noise of the radar system and the power of the received signal

Interferogram flattening

The generated interferograms have an almost linear phase trend across the image as a function of the slant range and baseline. Flattening of the interferogram consists of removing the phase component due to the variation of the range distance across the image. Removal of this phase term “flattens” the interferogram leaving fringes only related to changes in elevation (as well as noise, atmosphere and surface displacement). The operation is called flattening because in the case of a flat surface this would be the only component of the interferometric phase, under the assumption that the other components are null.

The interferometric phase variation can be split into two contributions:

1. A phase variation proportional to the altitude difference q between the point targets referred to a horizontal reference plane
2. A phase variation proportional to the slant range displacements of the point targets

$$\Delta\phi = -\frac{4\pi}{\lambda} \frac{B_n q}{R \sin \theta} - \frac{4\pi}{\lambda} \frac{B_n s}{R \tan \theta}$$

where θ is the radiation incidence angle with respect to the reference

It should be noted that the perpendicular baseline is known from precise orbital data, and the second phase term can be computed and subtracted from the interferometric phase(Esa).

Phase Unwrapping

The flattened interferogram provides an ambiguous measurement of the relative terrain altitude due to the 2π cyclic nature of the interferometric phase. The phase variation between two points on the flattened interferogram provides a measurement of the actual altitude variation. An integer number of 2π has to be added to recover the absolute phase difference. The process of adding the correct integer multiple of 2π to the interferometric fringes is called phase unwrapping (ESA).

Coherence

The quality of the phase difference of an interferogram is calculated from the degree of correlation between the interferogram pair. Essentially, interferometric coherence (c) is the measurement unit of phase noise and the ability of fringes appearing in an interferogram (Touzi *et al.*, 1999). The definition of cohesion (Born *et al.*, 1980; Hanssen, 2001):

$$\gamma = \frac{E[u_1 u_2^*]}{\sqrt{E[|u_1|^2]} \sqrt{E[|u_2|^2]}}$$

The coherence value ranges from 0 (the interferometric phase is just noise) to 1 (complete absence of phase noise). Very low values of coherence near to 0 correspond to a non-coherent image and very high values of coherence near to 1 correspond to a stable backscattered signal (Touzi *et al.* 1999). The quality of the interferometric phase is connected directly with the noise of the interferometric phase. Noisy areas are connected with low interferometric coherence and the opposite (Parcharidis, 2016).

The interferometric coherence is calculated by a number of parameters that characterized as noise sources of intrerferometric phase. The factors that affecting the final value of the interferometric coherence relevance are also indicate a reason / cause of decorellation of the intrerferometric phase (Hanssen, 2001):

$$Y_{total} = Y_{temporal} + Y_{geometric} + Y_{volume} + Y_{thermal} + Y_{processor} + Y_{Doppler}$$

where:

ygeometric = Difference of geometric acquisition between the two images

ytemporal = temporal decorrelation caused by natural changes on the terrain

yvolume = volume decorrelation when the scatterers are having a big size

ythermal = thermal decorrelation caused on specs of the antenna

Yprocessor = processor decorrelation based on the algorithm

yDoppler = Doppler centroid decorrelation

Total correlation is 1 when there is no decorrelation. The spatial baseline decorrelation is related to the horizontal separation between two satellite orbits (Osmanoglu *et al.* 2016). Doppler centroid related decorrelation effects occur when the satellite attitude (yaw, roll, pitch) is different during master and slave acquisitions. The effect is due to squint angle (Ψ), which is dependent on the yaw and pitch of the satellite (Miranda *et al.* 2003). Temporal decorrelation is stronger in forests where volume scattering is dominant and thermal noise of the radar is also an important decorrelation term, which is generally neglected for interferometry

As we mention InSAR can be used both for DEM reconstruction and the detection of surface deformation phenomena. However the observation for monitoring surface deformation is more challenging than it might seem because baseline-related to phase contributions cannot usually be neglected, phase noise and atmospheric effects hinder the estimation of actual displacement field affecting the area of interest.

5.5.1 Differential Interferometry (DInSAR)

Wherever a DEM is available, the impact of local topography on the interferometric phase can be limited by generating a differential interferogram (DInSAR). This processing estimates and removes baseline-related phase components. Using DEM of the area of interest and the information on satellite orbits, a synthetic interferogram is generated and subtracted from the original interferogram (Feretti, 2014).

The DInSAR technique uses interferometric InSAR methods to measure very small surface motions with high accuracy (1cm) in large spatial coverage areas (GABRIEL *et al.* 1989). In particular, the DInSAR technique exploits the phase difference, often referred to as interferogram, between two SAR images relevant to temporally separated observations of an investigated area and provides a measurement of the ground deformation projection along the radar line of sight (LOS) (Lanari *et al.* 2007).

Numerous applications for the type of instrument demonstrated, which can measure accurately extremely small changes in terrain over the large swaths associated with SAR imaging. The possibilities include accurate measurement of preseismic swelling and buckling and residual displacements from seismic events. Furthermore, this technique could be used to monitor long-term motion, possibly resulting in earthquake predictions (Gabriel *et al.* 1989). The DInSAR methodology has been applied first to investigate single deformation events (MASSONET *et al.*, 1993; PELTZER and ROSEN, 1995; RIGNOT, 1998). However, more recently, it also has been exploited to analyze the temporal evolution of the detected displacements via the generation of deformation time series. In this case, a time series of deformation can be solved through the inversion of an appropriate sequence of DInSAR interferograms.

5.5.2 Multi-temporal InSAR

Since the launch of ERS-1 satellite in 1991, archives of repeated SAR images over the same area became available, researchers started working at problems like DEM estimation via Multi-Temporal InSAR. In early 2000, the Polytechnic of Milan firstly proposed the Permanent Scatterers (PS) technique (Ferretti *et al.* 2001). The PS technique is based on the idea that, exploiting long series of SAR images, providing the opportunity to observe that height, displacement and atmospheric delay show different spectral characteristics as a function of normal and temporal baseline and as a function of space. However, the original PSI concept as published in (Ferretti *et al.* 2001) is very restrictive. A target is required to be coherent in all interferograms generated with a single Master image. Whilst urban areas usually are characterized by such features, it is very difficult to find them in other scenarios (as rural/deserted/mountainous areas). The need thus for increasing the density of coherent targets also in extra-urban areas brought to a series of improvements/generalizations of the original PSI algorithm. Some of this algorithms are SBAS, StamPS and Squeesar.

The main idea of multi-master approaches is to relax the strict conditions imposed by PSI techniques. Thus, instead of analyzing the InSAR phase generated with respect to a single Master image, more options can be considered. If the computational power is not an issue, all possible interferograms should be evaluated, searching for the coherent ones. Otherwise, subset of interferograms can be selected (as small normal baseline subsets or pairs that can guarantee the connectivity of the images graph (Perissin and Wang 2012)). In any case, in a multi-master framework does not refer any more to a single image. Moreover, in the single-master approach, the number of samples per equation in the periodogram was indicated as N_I (equal to the number of images and also to the number of interferograms). In a multi-master approach, the number of samples is equal to the number of interferograms N_{Int} , which is usually higher than N_I . DEM was removed from the interferometric phase and no initial phase unwrapping was applied. This analysis shows that Multi-Temporal InSAR can provide a more reliable phase unwrapping than working with single interferograms.

5.5.3 The SBAS Approach

As the Ferretti (2014) explains the Small Baseline Subset (SBAS) is a multitemporal interferometric technique that was the first of the second family of algorithms. It was developed by the CNR-IREA of Naples (Berardino *et al.* 2002) and it has been subject to changes and improvements to deal with both multilook (Lanari *et al.* 2007) and full-resolution interferograms (Lanari *et al.* 2004). The SBAS technique is a DInSAR approach allowing us to detect Earth's surface deformation and, to analyze their temporal evolution (Lanari *et al.* 2007). The characteristic of SBAS algorithm is rather than sharing a set of differential interferograms all sharing the same master scene, the SBAS works on interferograms having a normal baseline value significantly smaller than the critical one. Moreover, the baseline plot associated to SBAS is different, compared to the PSI techniques. The final target is always the estimation of displacement time series for as many points as possible, interferograms are calibrated using a common reference point and all differential displacements are referred to the first radar acquisition that therefore becomes an effective master image for the dataset. Despite the fact that all interferograms have a short normal baseline, possible DEM errors must be estimated and compensated for, as point out in Fattahi and Amelung (2013). The estimation of the atmospheric components is similar to what is performed in PSI techniques.

The main differences between SBAS and PSI techniques are (1) the procedure used to unwrap the phase data and (2) the type of scatterers used to estimate and remove atmospheric components (PS vs DS). The SBAS algorithm cannot provide useful information in phase data that cannot be unwrapped. In SBAS, the algorithm starts from M low baseline interferograms, filtered and unwrapped spatially. In general, $M > N$ and the baseline plot shows a fully connected network of points. It is then quite easy to estimate, for each DS exhibiting good coherence in the M available interferograms, N unwrapped phase values referred to the first image of the data-set, creating a time series of $N+1$ phase values, as the number of SAR data available. At least whenever phase unwrapping was carried out successfully on all M interferograms. The SBAS technique is applied pixel by pixel to all the areas exhibiting a sufficiently high coherence degree and is robust with respect to possible errors of the DEM used in the derivation of the differential interferograms. (Berardino *et al.* 2002).

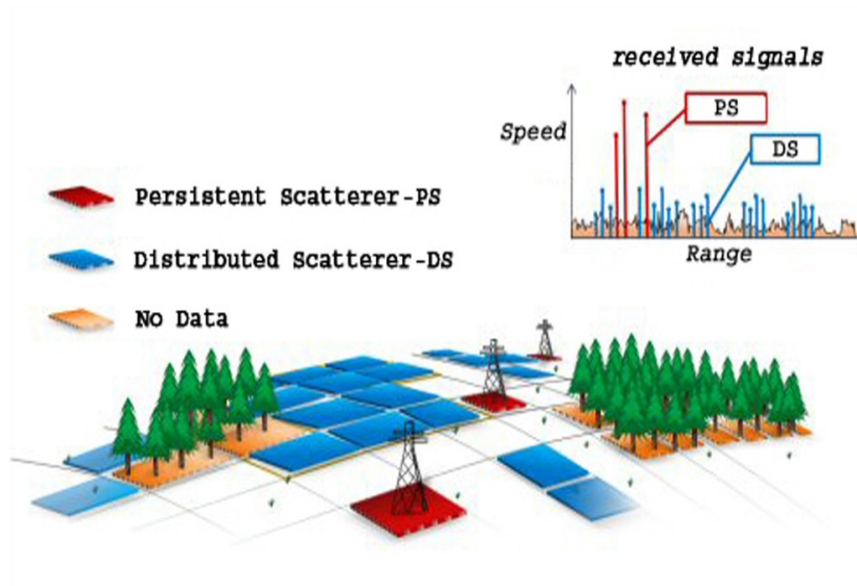


Figure 13: PS and DS scatterers.

Distributed scatterers (DS), exhibiting fairly good coherence in some interferograms, are identified from the homogeneous ground, scattered outcrops, debris flow, non-cultivated lands and desert areas, while PS typically correspond to man-made structures, exposed rocks, outcrops and boulders. DS is characterized by lower reflectivity values compared to PS, but their information content can be improved by spatially averaging neighboring samples (Ferretti, 2014).

6. Data and Methodology

6.1 Data

A dataset of 241 Sentinel A & B, TOPSAR C-band, in the Interferometric Wide Swath (IWS) data acquisition mode covering the period 03/2015 to 10/2020 was downloaded from Copernicus Open Access Hub (<https://scihub.copernicus.eu/>) to monitor the surface subsidence through the investigated time period.

For this dataset, two stacks of 118 and 123 SAR scenes, acquired in ascending and descending mode along track 102 & 7 respectively, were used for a multi-temporal analysis to produce two layers of surface deformation in the line of sight (LOS) and two of displacement decomposition (vertical and east-west) along the plain over the last six years, from March 2015 to October 2020.

In addition, an acquisition of high spatial resolution satellite images were acquired by COSMO-SkyMed (CSK) spacecrafts, in order to produce results of higher occurrence. Due to the fact that the CSK have't acquisitions for the area of interest before the August of 2019, 72 images were collected until January 2021. It should be mentioned that only the 66 were used due to unsolved problem of software.

Meteorological data of rainfall and average heat collected from two local weather stations of the National Observatory of Athens during 2015-2020 in order to correlate the subsidence trend with dry and wet season.

6.2 Methodology

The present study is an attempt to use remote sensing and data for monitoring the southern Larissa plain deformation in a specific time period to investigate the surface subsidence trend after the recharge of Karla lake. The workflow is presented in next page. The goal is to obtain the crucial data needed to reach justified conclusions regarding the surface subsidence and provide useful directions for further investigation if needed. The first step of the workflow is the data acquisition, which includes data regarding the satellite image dataset, the temperature, the rainfall records and GNSS data for validation purposes. The second step includes the data processing, which is performed on SARscape ENVI software, using earth observation and environmental data. In this step, multi-temporal SAR data processing was carried out following the Small Baseline Subset (SBAS) algorithm using a multi-reference stack of pairs of SAR SLC images to create a multi-reference baseline network of interferograms with the more as possible combinations between the available images. Finally using meteorological data to contribute to the interpretation of the displacement data processing results. Based on the conducted processing and calculations, surface deformation plots and maps are generated. The results are qualitatively validated using GNSS data. In the Displacement Decomposition step, the displacements of study area are recovered into the vertical and horizontal components to explain the displacement observed in the Light of Sight (LOS). A large number of interferograms were obtained, specifically 398 Sentinel-1 pairs (mean absolute baseline 61 m) in ascending mode and 422 Sentinel-1 pairs (mean absolute baseline 53 m) in descending mode as well as 396 CSK pairs (mean absolute baseline 173 m) in ascending mode.

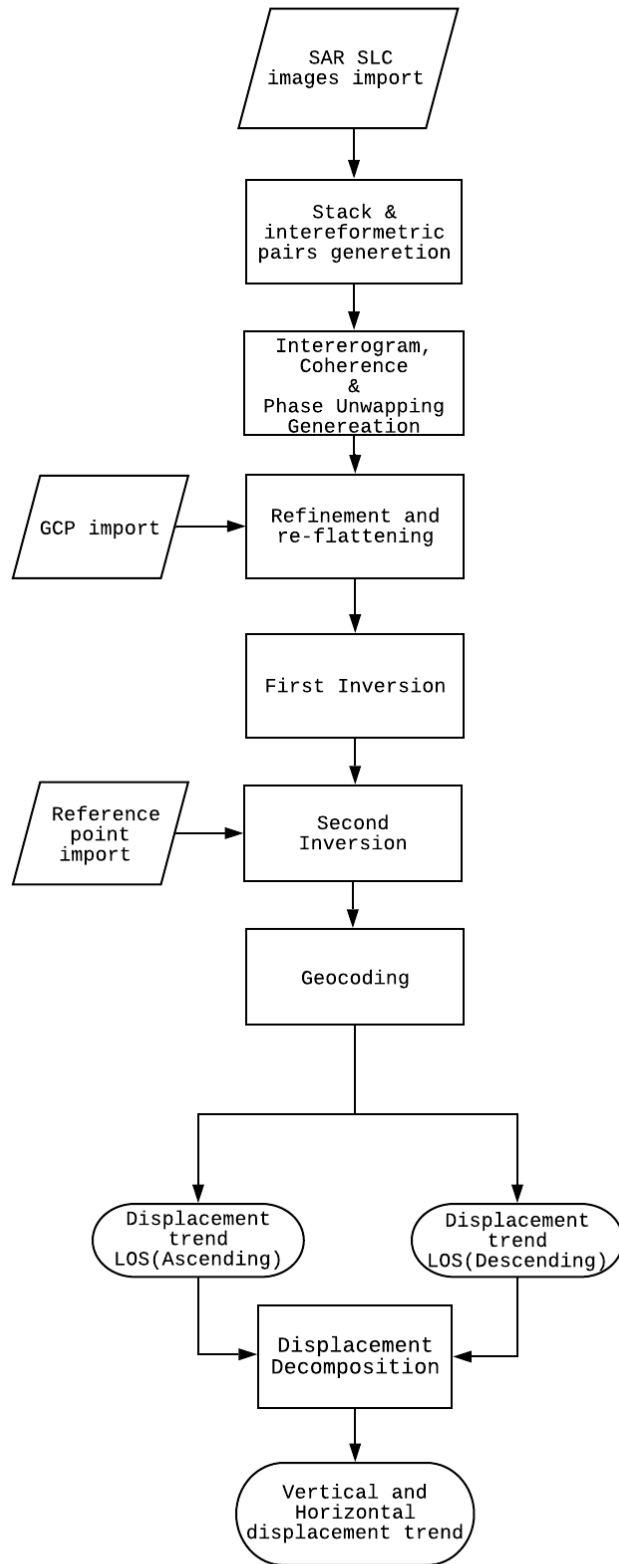


Chart 1: Flowchart on interferometric processing

Data import

Firstly, the preprocessing step includes splitting each sub swath with the selected bursts to cover the area under study and orbiting the refinement using the precise orbit files. On this step, the VV polarized Single Look Complex (SLC) level-1 SAR scenes and the specific burst from kmz file which determines the area of interest were selected. As the land displacement area is known and it is a small part of the whole frame coverage, a subset of all images has been produced in order to reduce the processing time and the hard disk usage.

Image Stacking

At this step, a comparison between scenes will be applied in order to create interferometric pairs. These pairs will correspond to a stack of wrapped interferograms. The Master image will be automatically chosen from the software and all the processed slant range pairs will be co-registered on this reference geometry. We avoid choosing manually the reference Master image because, according to SARscape manual, it could be the risk of retrieving fewer connections. For this study, small temporal baseline pairs (60-days) and perpendicular baseline (mean ascending 61 m , mean descending 53 m) were selected in order to avoid losing the spatial coherence for Sentinel-1 data (2015–2020). As a result of this step, we get an auxiliary file that includes information for the stack of wrapped interferograms and two plots of Connection Graphs which shows if the network of pairs is well connected. At the Figures 14 we can see that our graphs are homogeneous and every acquisition is connected with others with a high redundancy (min acquisition > 5).

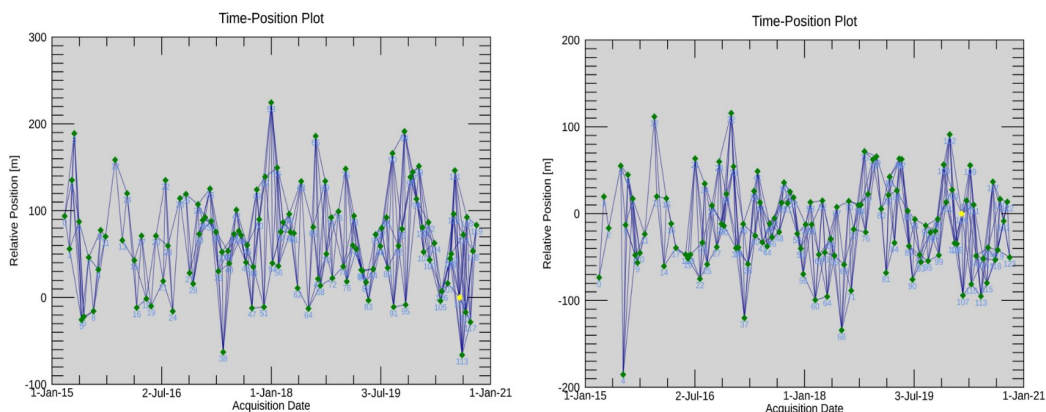


Figure 14: Connection graph showing perpendicular and temporal baselines of SLC pairs relative to the master image: (Left) Sentinel-1 Ascending mode (master: 30 July 2020), (Right) Sentinel-1 Descending mode (master: 25 February 2020).

In the case of the CSK data, different parameters have been set. In order to have a well connected graph with the best possible connections, the temporal baseline set to 180 days and the max normal baseline up to 390 m. Moreover a triangulation connection graph have been generated in order to have a more balanced network.

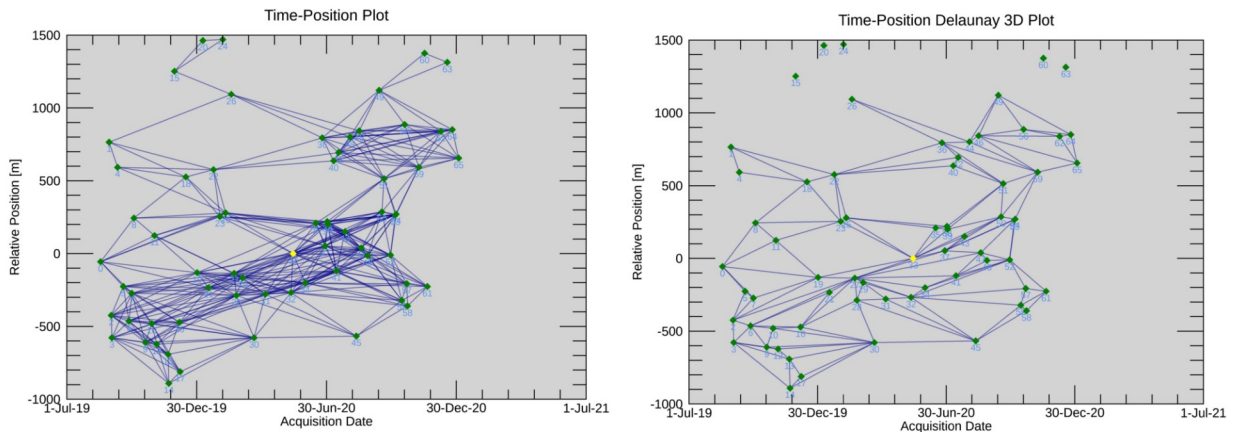


Figure 15: Connection graph showing perpendicular and temporal baselines of SLC pairs relative to the master image for COSMO – SkyMed data in Ascending mode (master: 14 May 2020), (Left) 2D connection, (Right) triangulation connection.

Interferometric Process

During this step, each pair of images, identified in the image stacking, is used to generate interferograms. At this stage of processing, it is important to define the slant range multi-looking for the interferogram generation. Multi-looking in azimuth and range (1×4 for Sentinel-1 and 3×3 for CSK) was applied to mitigate phase noise, and NASA's 90 m resolution Shuttle Radar Topography Mission (SRTM) Digital Elevation Model (DEM) was used to subtract topographic phase components and for corregistration of slave images with master image. A Goldstein adaptive filter was applied to the interferograms to reduce the phase noise (Goldstein and Werner 1998). The generated interferograms were unwrapped using the Minimum Cost Flow (MCF) algorithm. The low coherence values can produce particularly noisy areas in the analysis, which decreases the reliability of the results. Due to this fact, a coherence threshold is set at 0,3. Areas having coherence lower than the threshold value will be not included for further processing.

Refinement and re-flattening

This step is executed to estimate and to remove the remaining phase constants and phase ramps from the unwrapped phase stack. For the purposes of this step, Ground Control Point (GCP) must be produced for refinement. The GCP can be selected either in slant geometry (range and azimuth) or in geocoded geometry. Moreover, GCPs location should respect some general criteria. The location of GCPs must be selected on flat and stable zones with high coherence values so these criteria should be valid for most of the interferograms contained in the stack.

Inversion First Step

At this phase of processing, a first estimation of the displacement rate and the residual topography is calculated. Moreover, a second unwrapping is done within this stage on the input interferograms to refine and improve the input stack in view of the next step. For the estimation of the displacement rate, we choose the linear inversion model. Linear model is the most robust inversion model compared with the other models which require high connection graph redundancy and high coherent interferograms to provide reliable results.

Inversion Second Step and Geocoding

This step implements the inversion kernel to retrieve the final displacement time series. Atmospheric filtering is applied on displacement time series of the previous step in order to recover the final and cleaned displacement. At this step, a GCP is used to remove a residual phase constant. The final results will be referred to this GCP which is referred as a reference point. The selection of the reference point is an important part of the analysis, as the final deformation rates are greatly affected by that selection (Parcharidis et. al, 2010). For this reason, the reference point must be chosen very carefully on an area that is already known as stable for all the time period. The average of coherence, which is generated over the stack processing, was used in order to choose a high-quality region as a reference. For purpose of this study, the reference point is selected on the settlement of Megalo Monastiri with a coherence value of 0.88 for ascending and 0.90 for descending. The reference point is the same for both geometries in order to have comparable results. As the Figure 17 shows, the reference point is stable for all the period of this research. The results for this step takes into account a coherence

threshold on the input stack of the unwrapped phase. Only the pixels which are over the threshold in most of the stack will be solved by the inversion. The generated products of displacement and velocity are geocoded from slant range format into geocoded images with coordinate system and same pixel size. The result is a geocoded image based on the coordinate system WGS 84.

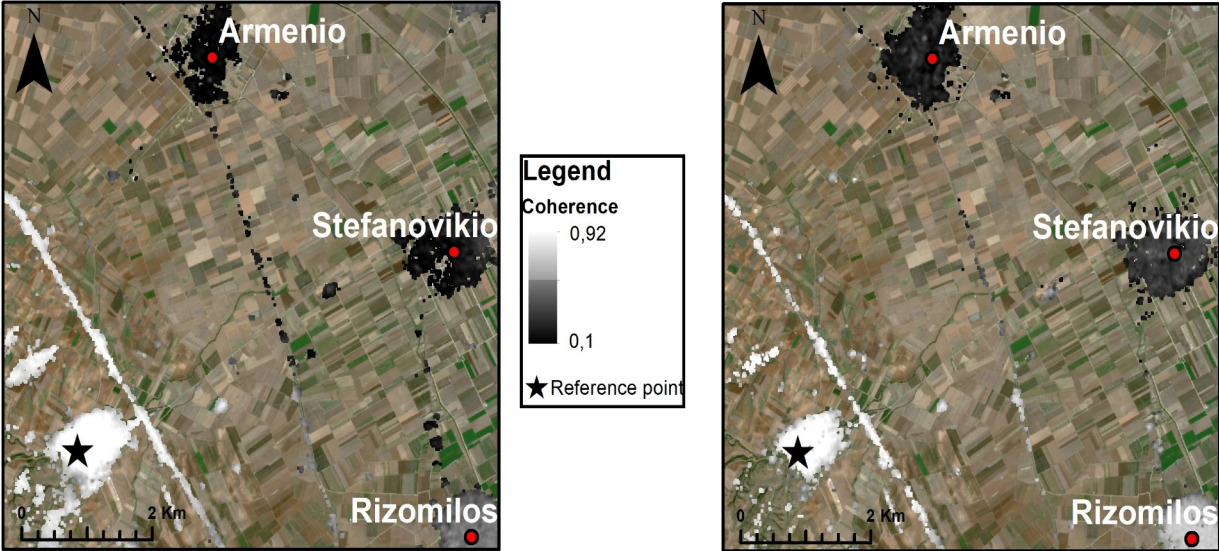


Figure 16: Coherence maps for ascending(left) and descending(right) geometry of Sentinel-1.

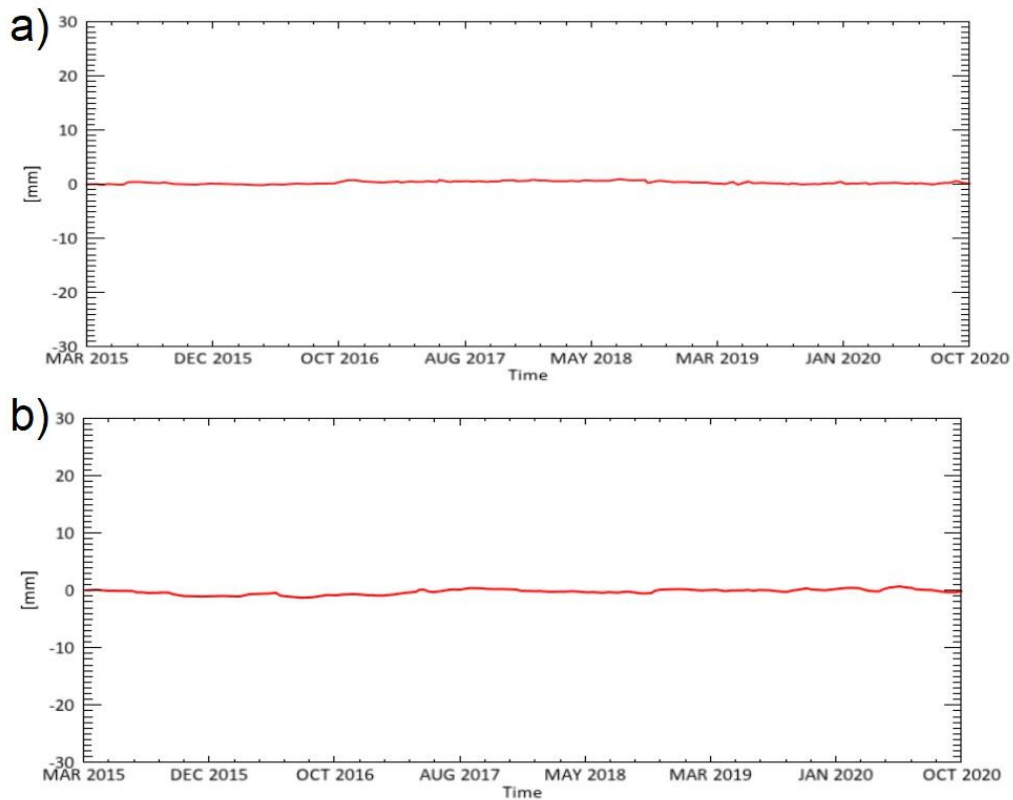


Figure 17: Time series plot for reference point ascending(top) and descending(down)

Estimation of vertical and horizontal displacement

Finally, the Displacement Decomposition is applied to generate the vertical and east-west components for both the displacement time series and average velocity. It requires two different acquisition geometries to retrieve the displacement of vertical and east-west components. These layers have been generated only for Sentinel-1 products because we have only one geometry for CSK data.

7. Results

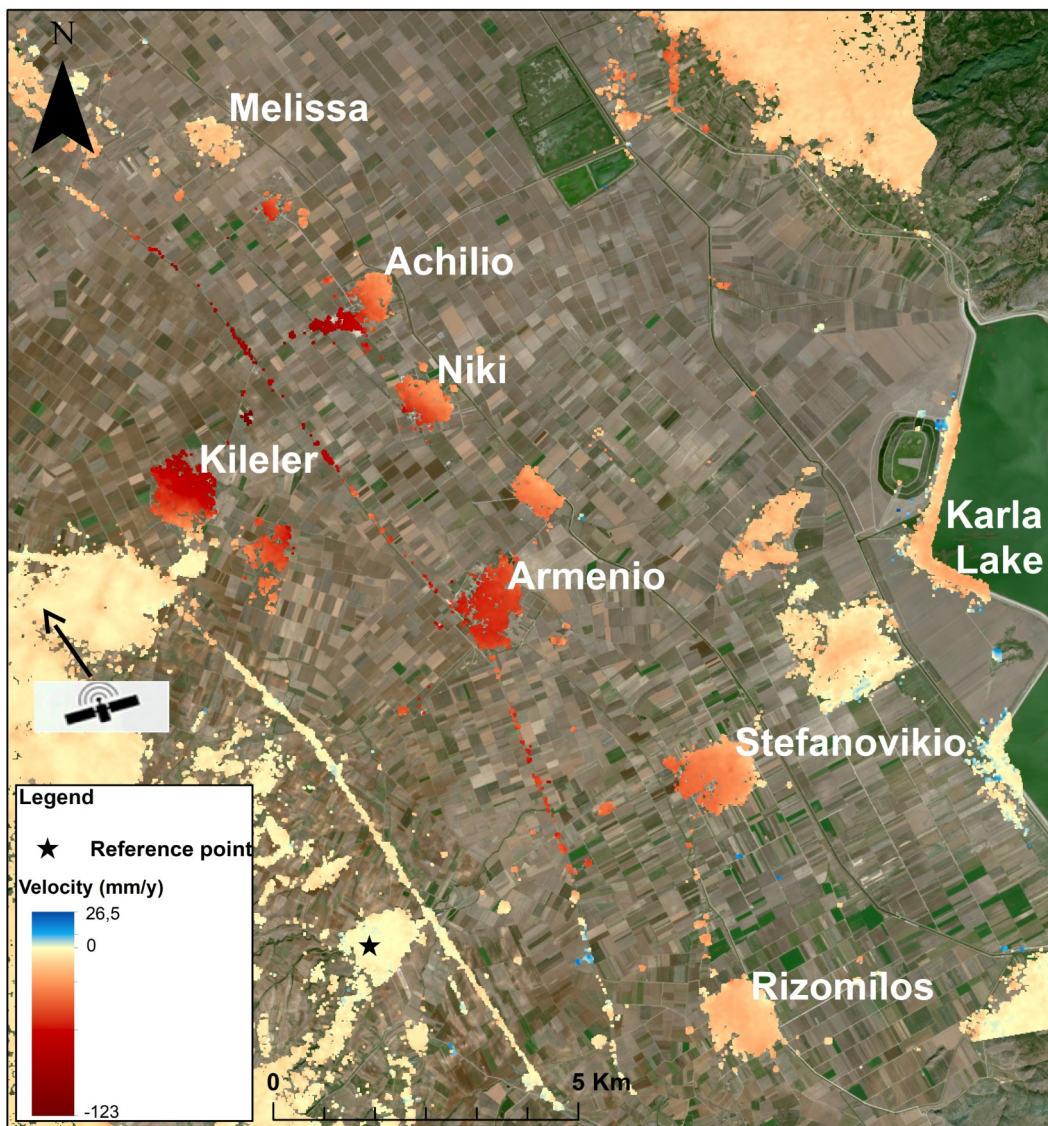


Figure 18: Average deformation trend for Ascending Sentinel-1

The Average deformation rate (mm/yr) (LOS ascending, descending) determined from Sentinel-1 SLC data between March-2015 and Oct-2020 (Figure 18) showing that the area subside. The most of the scatters are identified on the built-up areas, roads-railroads and rocks which showing more coherence. The displacement maps in LOS are having quantitatively differesces on the NE side of AOI, showing uplift up to 26,5 mm and down lift up to -123 mm along the ascending dataset and 38,5 mm and - 95 mm in LOS respectively for the descending respectively (Figure 19).

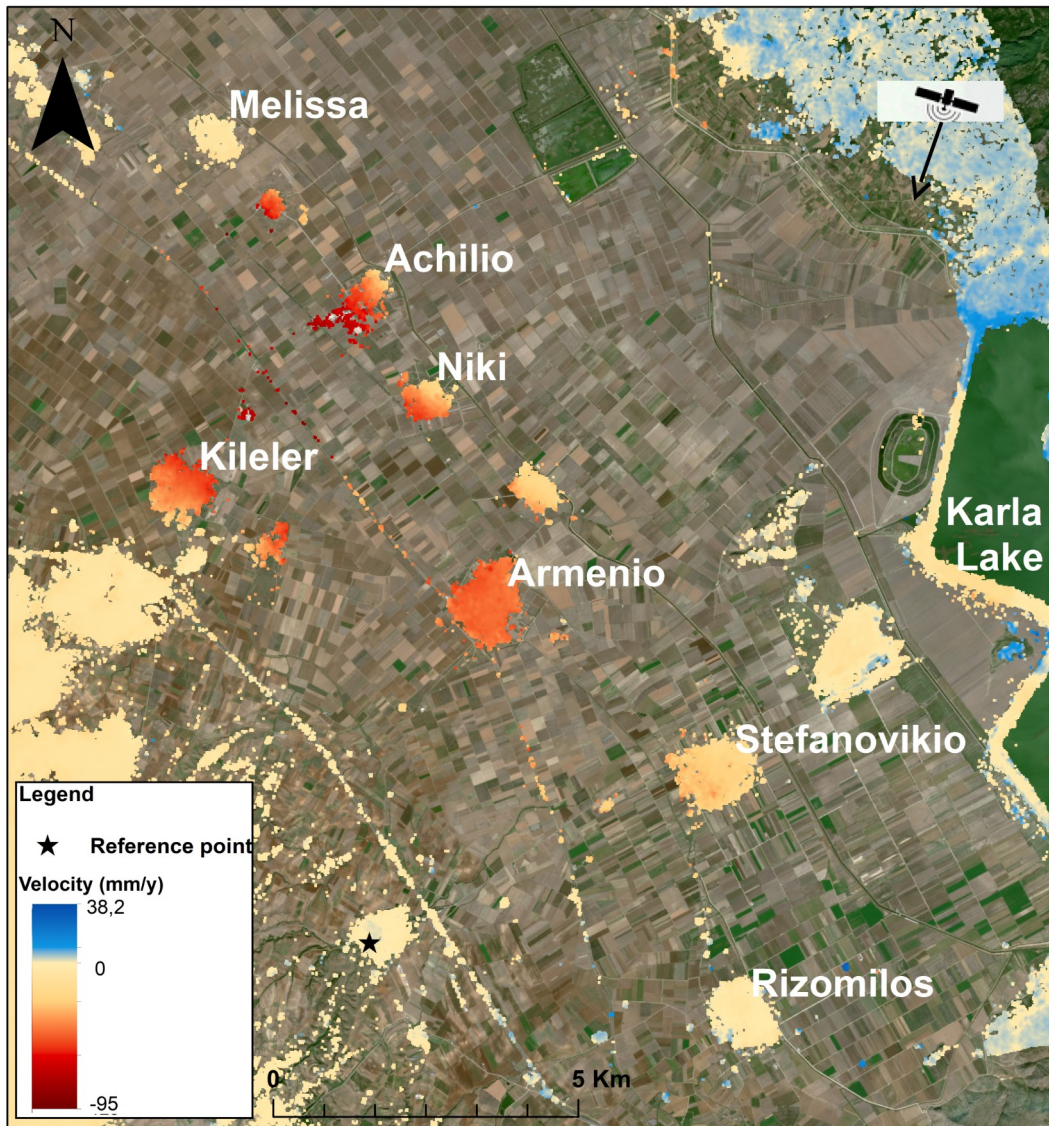


Figure 19: Average deformation trend for Descending Sentinel-1

The higher trends are detected in the center of Larissa plain with Kileler, Armenio and Achilio villages affected the most. The main difference of the two LOS is detected on the NE side of AOI with ascending geometry recording negative movement and descending geometry positive movement respectively. This difference is recovered on the displacement decomposition as a horizontal movements with opposite directions which we will discuss later in this section. Specifically there are villages that observed high rates of subsidence with very interesting deformation patterns.

To evaluate the subsidence behavior, distance-displacement graphs were created taking into account sections, constructed based on the ascending velocity map. More specifically, three sections (A1-A1' to A3-A3') and the corresponding graphs were obtained with direction from west to east (Figure 20). The sections and the corresponding graphs were constructed in three settlements, where higher trend rates and damage reports occurred. As the Figure 20 shows, for sections A1-A1' and A2-A2' the highest subsidence trends are located in the western part of the settlements and decreases as we head east towards to Karla lake. In contrast, section A3-A3' the lowest values being located in the western part of the settlement and increasing towards the eastern part. The Stefanovikio settlement showing interesting subsidence pattern with high rates of subsidence almost -38 to -30 mm/yr on the west part of the village and the other part follow with less subsidence up to -25 to -20 mm/yr. The same deflation pattern identified at Armenio settlement reveals a higher subsidence from -55 mm/yr to -35 mm/yr. The Kileler settlement has an opposite deformation pattern with the east part showing less subsidence up to -35 to -40 mm/yr and west part a higher subsidence rate up to -77 m/yr and -50 mm/yr. Summarizing the observed deformation behavior we can identified that there is existing more subsidence at the center of the plain. Maybe the distance between the settlements and Karla lake (quantity of underground waters) or stable ground (mountains) can describe this deformation pattern around the plain.

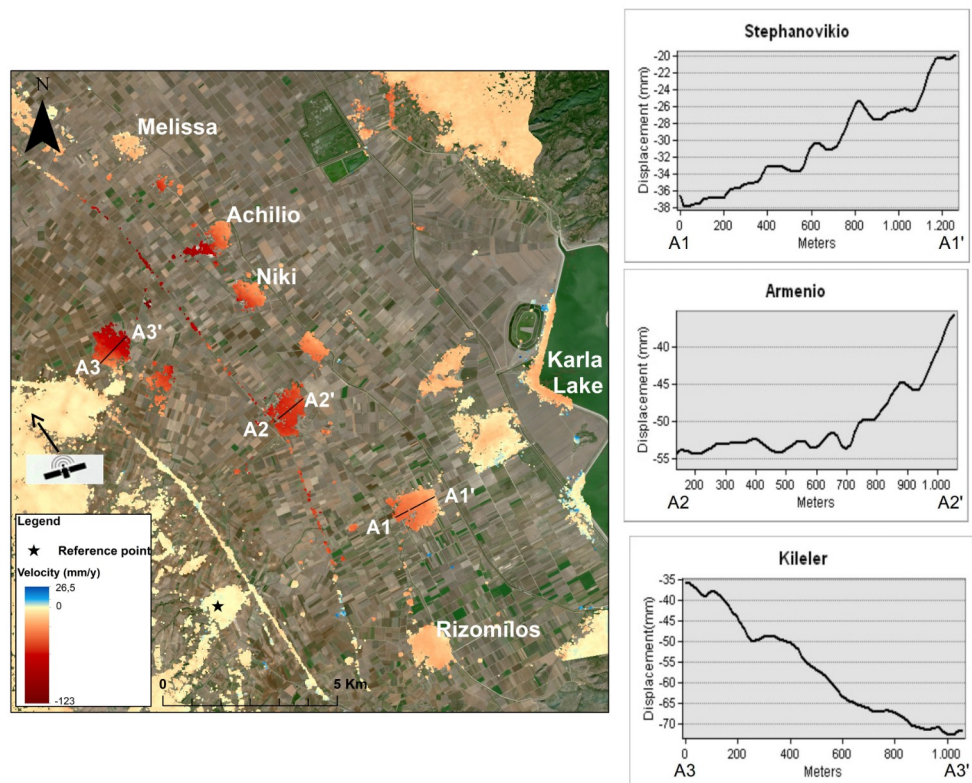


Figure 20: Cross sections in Ascending mode using Sentinel-1 products.

Analyzing the deformation time series from Sentinel-1 SLC ascending geometry data between March-2015 and 25-Oct-2020, we can identify the cumulative historical deformation patterns (Figure 21). Locations over Thessaly plain were selected and grouped in three domains to understand the deformation pattern behavior of the area. At the domain A of Figure 21, the time series of scatterers at the Stefanovikio showing a low subsidence rate (P1, P2, P3, P4) at the east part of the settlement which are increased as we move to the west part. At domain B, Armenio and Sotirio settlements identified that rates of subsidence follows the same pattern with domain A. The scatterers P5-P6 on the domain B are located at the center of the basin showing higher cumulative rates of subsidence on the time series comparing with domain A and have more similarities between Sotirio (P7,P8) and the eastern part of Stefanovikio (P3). The same patterns were identified at the C area with the scatterers (P9,P10,P11,P12) displaying cumulative downlift rates motion on the time series. The subsidence pattern based on time series analysis seem to agree with the results of the sections showing that the subsidence is higher at the center of the plain. An additional remark is that the seasonal deformation signals are more intense on scatterers that located closer to the center of the basin and having high subsidence rates than the others which their times-series are showing linear rates.

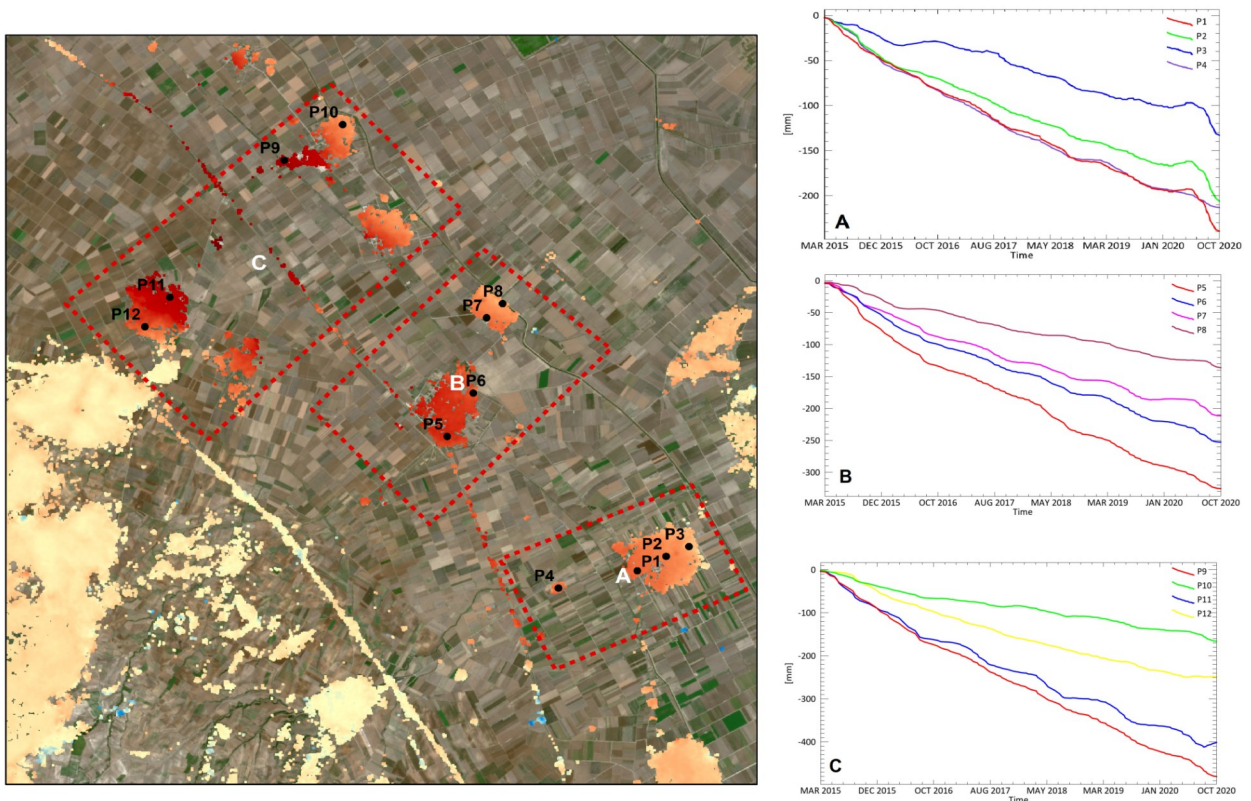


Figure 21: Deformation Time Series from SBAS using Sentinel-1 data between Mar-2015 and 22-Oct -2020 over Thessaly plain, Greece.

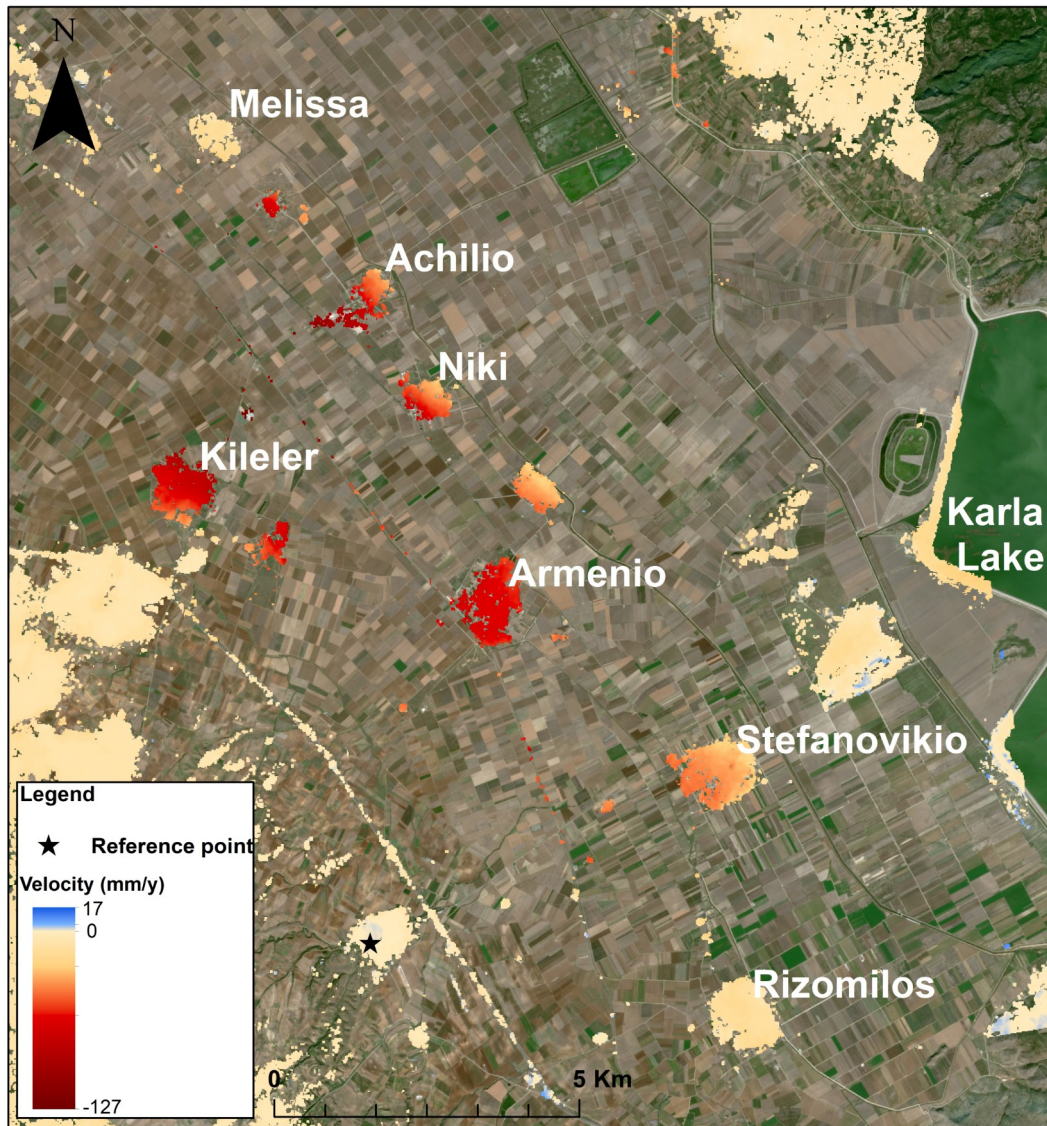


Figure 22: Average deformation trend on Vertical after displacement decomposition of two geometries for Sentinel-1 data.

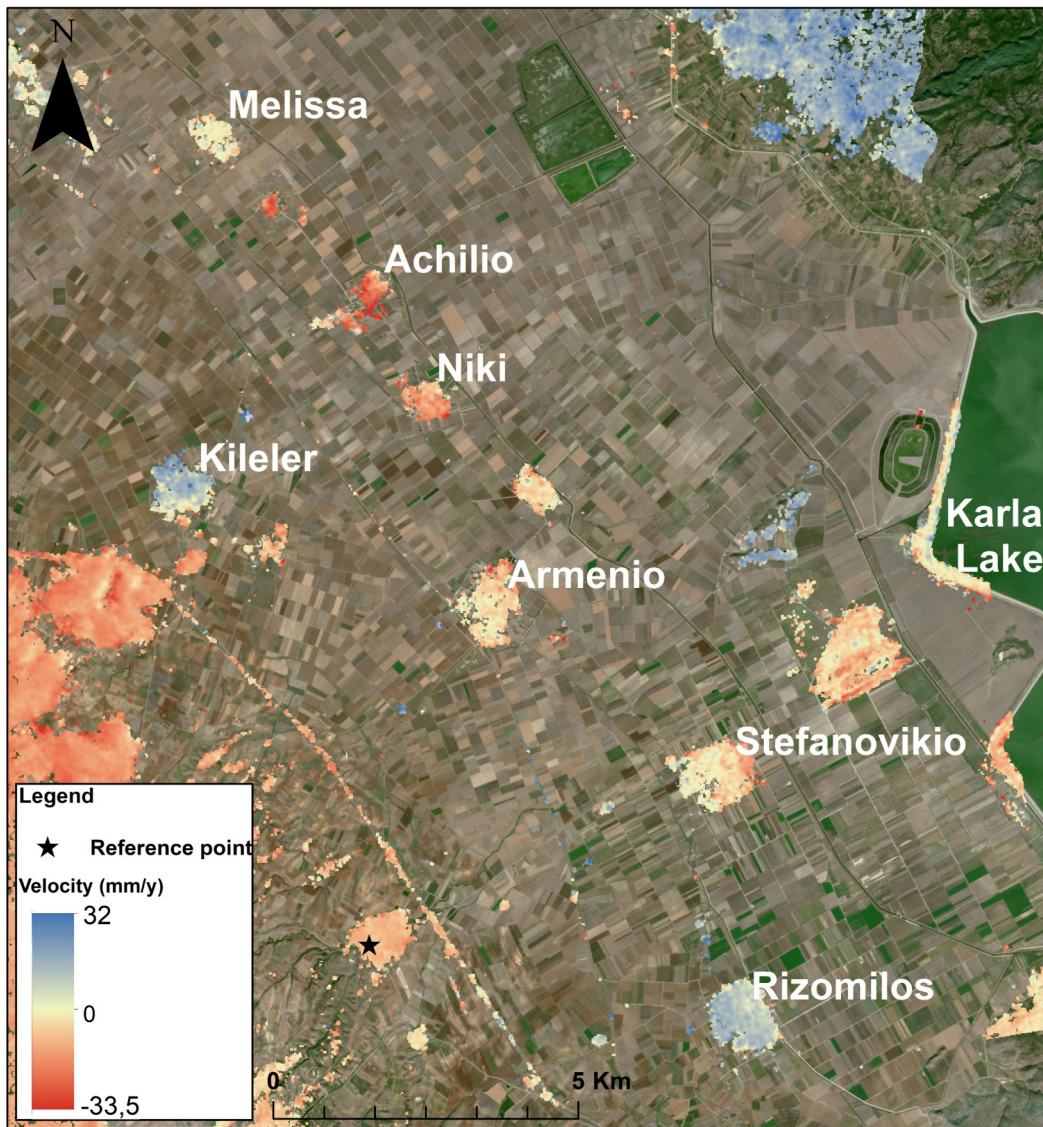


Figure 23: Average deformation trend on East-West after displacement decomposition of the two geometries using Sentinel-1 data.

Displacement Decomposition results show that in the vertical (up-down) displacement (Figure 22) positive values mean upward up to 17 mm and negative values downward up to -127 mm. For the horizontal (east-west) displacement map (Figure 23), positive values mean eastward up to 32 mm/y and negative values westward up to -33,5 mm/y. The subsidence trend of vertical displacement map follows the same pattern of motion of the two geometries on the center of the study area and decrease as we move toward to the Karla lake and stable ground (mountains). On the horizontal displacement, the villages are stable having small movements to the west, with the exception of Kileler and Rizomilos settlements which their movement is opposite. Very interesting are the movements that detected on the east and west perimeter of the study area. This result shows us that the normal faults activated during the Pliocene-Lower

Pleistocene which generated the NW-SE trending of Larissa Basin (Caputo *et al.*, 1994) are still active and affecting the morphology of study area (Figure 5).

Furthermore, the mean average subsidence trend was collected for the five main settlements of the basin: Stefanovikio, Kileler, Armenio, Achilio and Rizomilos. According to the Figure 24, the settlements with the highest trends are Kileler and Armenio which are located closer to the center of the Larissa plain.

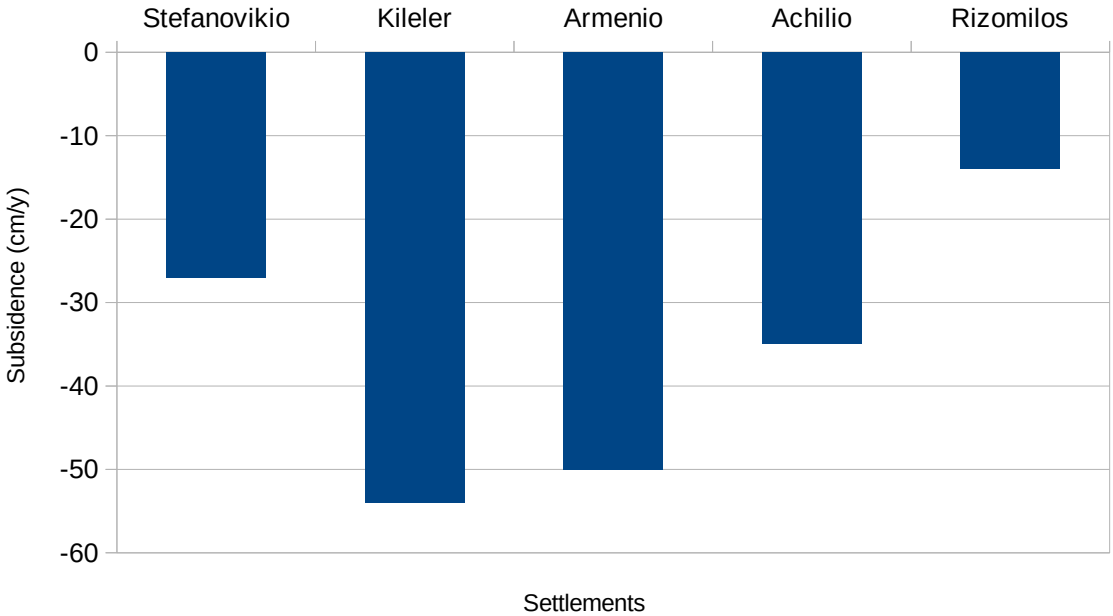


Figure 24: Bar plot showing the mean average subsidence trend for the five main settlements of study area.

Comparison with GNSS station

A comparison of the SBAS results and GNSS data (STEF00GRC) of National Observatory of Athens was carried out, using the closer scatterer in the location of the station (lat: 39.464, lon: 22.742). The GNSS data based on the results of Argyrakis *et al.* (2020) covering the period of 2013-2017. In order to compare the results, we focus on the same period of both studies (2015-2017). The DInSAR displacement time series plot based in the product of vertical displacement which is generated from displacement decomposition. Comparing the results, the time series seems to qualitatively agree with quantitative differences. Both results follow continuous subsidence which is more intense during the dry periods for GNSS products. The difference between the results is relative high. DInSAR products show a cumulative displacement up to -12 cm while the GNSS products showing around to -22 cm. This discrepancy can be caused due to many factors such as the inaccuracy of coordinates, the processing of satellite data as well as the infrastructure on which the GNSS station is located. Further examination of this problem is suggested.

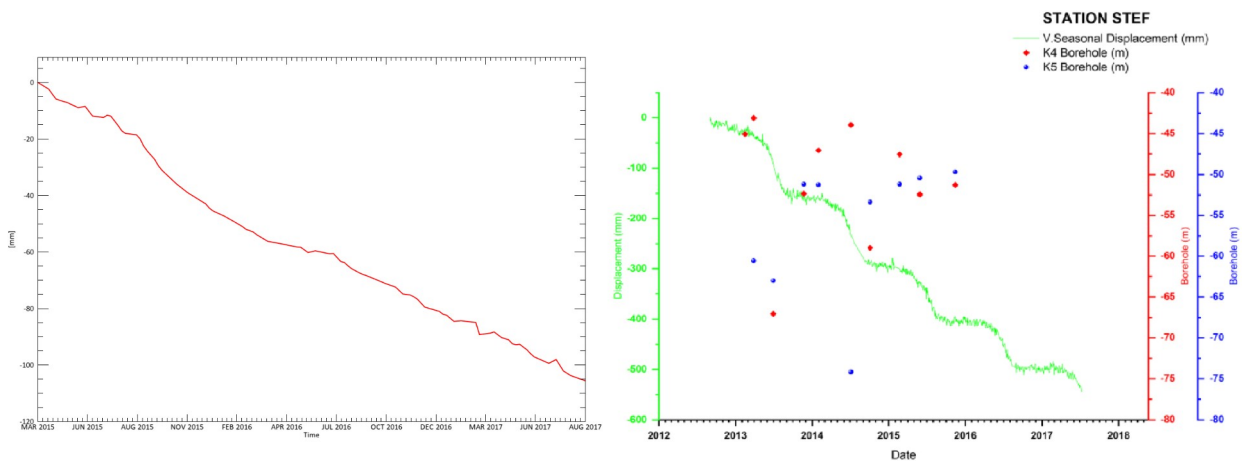


Figure 25: Comparison of cumulative times-series on vertical displacement with GNSS station in Stefanovikio(STEF).

Comparison with previous studies

In this study, an acquisition between 2015-2020 using Sentinel-1 SLC data, was carried out. In order to understand if the recharge of Karla lake has affected the subsidence trends, a comparison of the results with previous studies on southern Larissa plain is required. In Figure 26 showing the difference of higher trend velocities that have been detected in this master thesis and previous research (Benekos et al. 2014) using ALOS – PALSAR SLC data for the period 2007-2011. Comparing the higher trends of five settlements, showing that the recharge of Karla lake affects the subsidence rates for all the settlements except Kilelelr which is the most distant from the lake. The significant differences at Stefanovikio (8 mm/y) and Rizomalos (4 mm/y) settlements showing that recharge of Karla lake has a big impact on the groundwater deposits close to the lake.

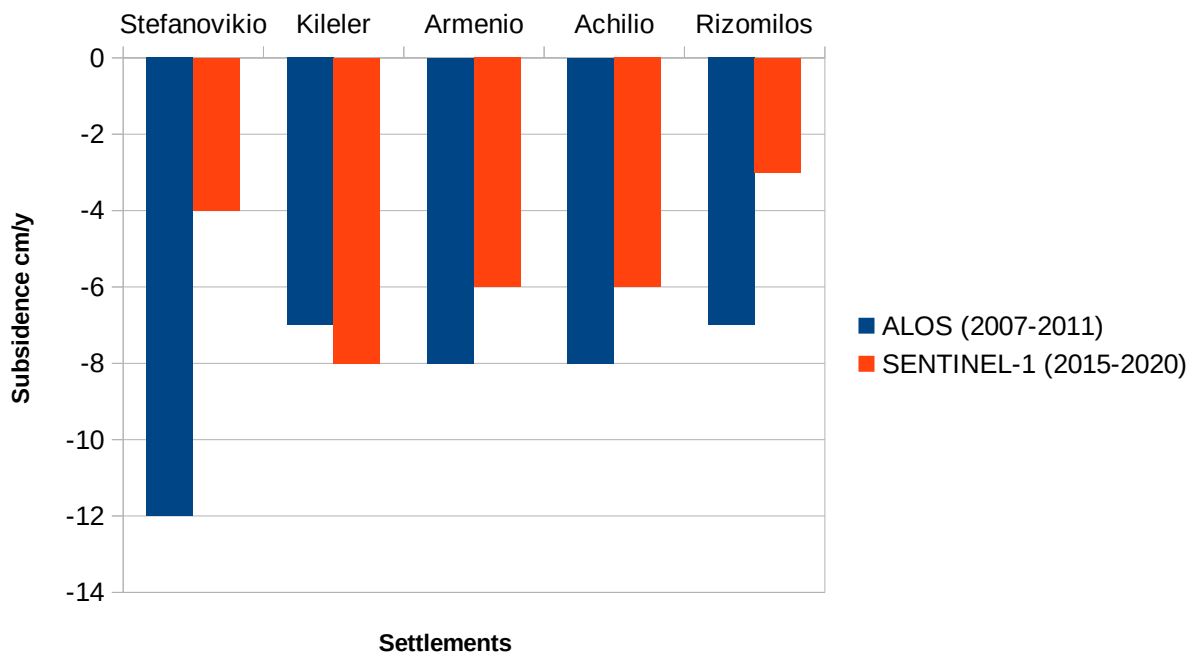


Figure 26: Barplot showing the change of high values of subsidence trend by comparing results of this thesis with a previous research on the same area.

Another comparison of cumulative subsidence of scatterers shows the change of subsidence pattern after the recharge of Karla lake in the study area from the southeast to the center and north (Figure 27). A number of scatterers based on study of Benekos et al. 2014 have been used in order to estimate these changes. As their study shows the cumulative displacement in diagrams and not as specific numbers, the determination of the values is approximate. According to Figure 27, the subsidence rates have been reduced for domain A (P1,P2,P3,P4,P5)

which was the most affected area for period 2007-2011 and increased for domain B and C (P8,P9,P10,P11,P16, P17,P20) with the higher rates detected on Kileler settlement. Domain A is the closest on Karla lake showing that the recharge seems to have an effect on groundwater aquifers and consequently on land subsidence. Although the Figures 26 and 27 seem to be in conflict about the Achilio and Armenio, that does not negate the fact of the general increase of subsidence for these settlements as are refers as individual points

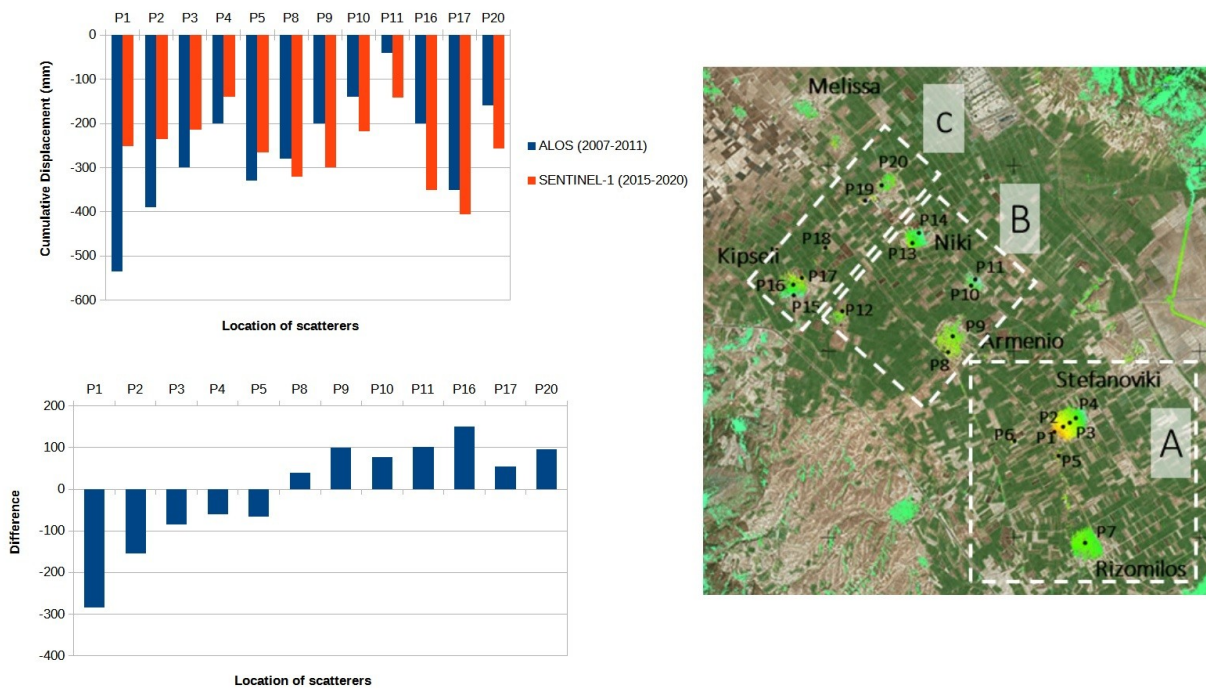


Figure 27: Comparison of cumulative deformation from PS(ALOS PALSAR 2007-2011) and SBAS (Sentinel-1 2015-2020) data. The image contains modified data of Benekos et al. 2014.

Furthermore, comparing on another research (Foumelis et al. 2016), for the time period of 2002-2010 using ERS and ENVISAT SLC data, the recorded subsidence trend was up to 15-20 mm/year while in this master thesis is up to 14-17 mm/year, verifying that the subsidence trend is actually decreased.

CSK products

The CSKs products seem to follow the same pattern as the Sentinel-1 results. Areas located in the center of the plain show higher subsidence rates in contrast with the rest areas that located closer to the lake and on solid ground.

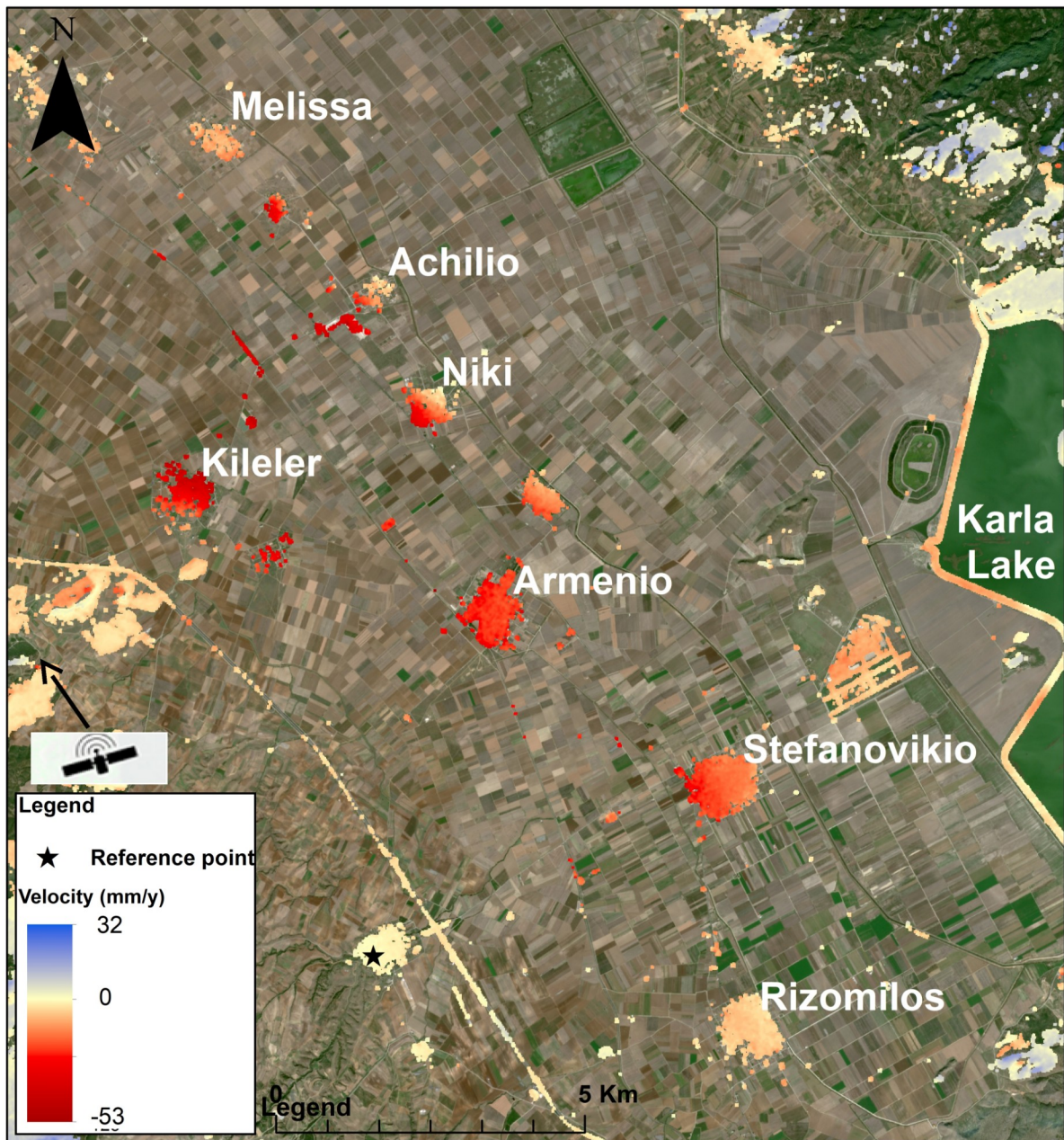


Figure 28: Map of average deformation trend in ascending mode based on CSK data.

The settlement with the highest subsidence trend is Kilerer which reaches -52 mm/y in the eastern part and decreases as we heading to the west side. Next is Armenio settlement with highest subsidence rate up to -35 mm/y. The settlement seems to be characterized by a uniform distribution of subsidence throughout its area with a slight decrease to the east. High values of subsidence trend up to 34 mm/y are also detected in the western part of Stefanovikio and Niki, with a decrease of subsidence towards the eastern part. The same pattern is detected the rest of the settlements (Sotirio, Kokkines) with lower subsidence rates. Exception is Rizomilos settlement, as in the results of Sentinel-1, are relatively stable with low settling rates of up to 14 mm/y.

Histograms were created for the three largest settlements. The histograms show the fluctuation of subsidence, as well as the frequency of values, across the settlements. For the settlements of Stefanovikio and Kilerer, which follow a similar pattern of subsidence, this value fluctuation is shown in their histogram. Stefanovikio values are recorded with a higher frequency up to -30 to -10 mm/y, with the highest values being detected in a small number of scatterers. Similar behavior detected on Kilerer with a higher appearance of scatterers who corresponding to the maximum values (-50 mm/y). Armenio settlement is characterized by uniformity of subsidence all across its borders. The values that are mainly detected are in the range of -30 to -20 mm/y. Larger or smaller values of subsidence are minimal.

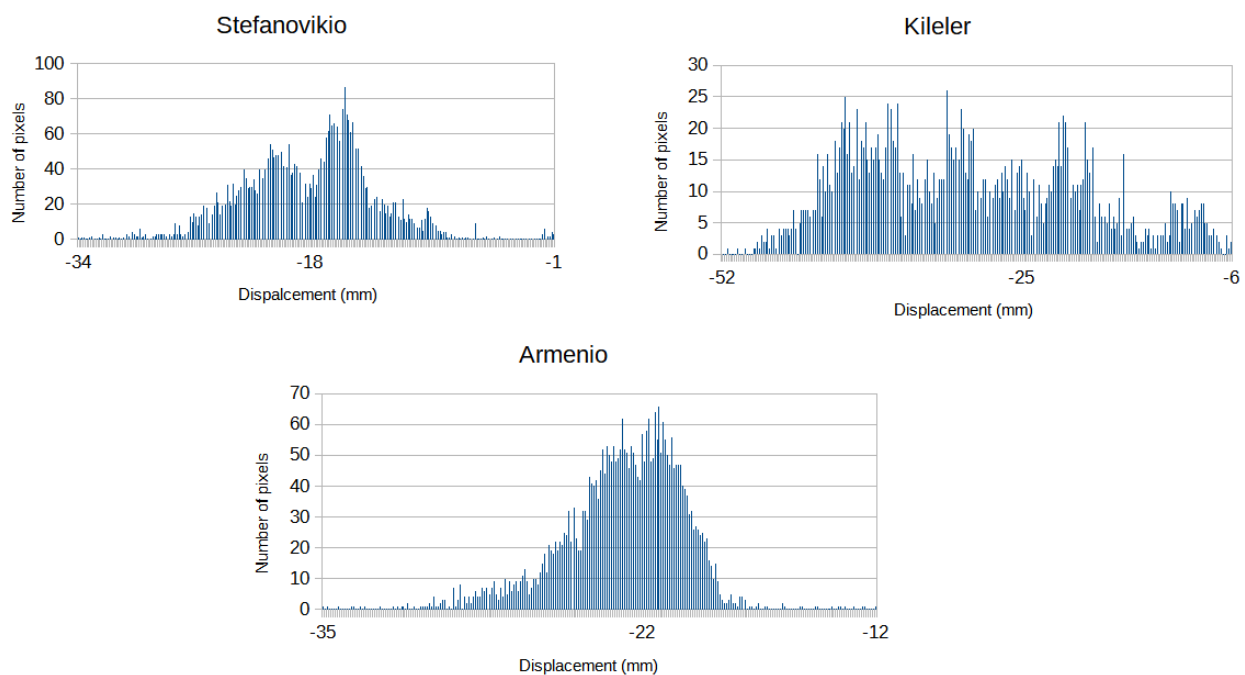


Figure 29: Histograms for the three biggest settlements.

The comparison of the average annual trend for the five main settlements was carried out, using final products of the two satellite systems in ascending mode. In the Figure 30, it is clear that there is a discrepancy in the satellites observations up to 30 mm for the settlements that characterized from high subsidence rates, while there is a higher agreement in locations where the subsidence rate is low for both satellites.

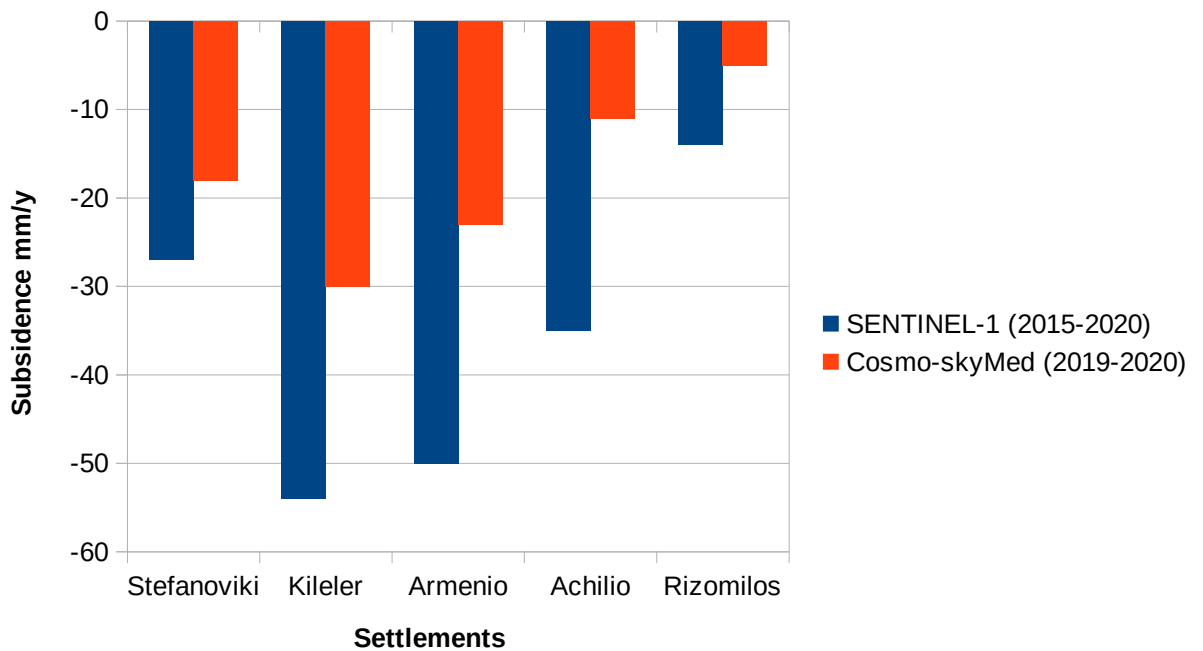


Figure 30: Comparison of mean subsidence rate between five settlement using Sentinel-1 and CSK products

Despite their quantitative differences, the results seem to detect the same pattern of subsidence in the center of the basin. The Sentinel-1 products recorded higher rates in general. The CSK results are showing more clearly the seasonal deformation than Sentinel-1. The differences between the two satellite system can be caused due to the spatial resolution – accurate, the wavelength, processing parameters (temporal threshold, resample grid size), the temporal length possible affecting the calculations.

Correlation of subsidence and dry-wet seasons

The combination of deformation products and meteorological data can prove that there is a strong correlation of precipitations and higher subsidence rates. According Parcharidis *et al.* 2011, seasonal deformation signals are expecting to be detected during the dry seasons. As we mention on the time series results, the seasonal deformation rates are more intense on locations closer to the center of the basin with high subsidence trends. In order to detect those signals we focus on areas which are characterized by this criteria (Figure 31). On the time-series plot of Stefanovikio settlement we detected higher subsidence rates during the dry seasons which is decreased on wet seasons. A barplot combined rainfall/subsidence shows that decrease of rainfall during the dry seasons following by an increase of subsidence rate.



Figure 31: Map of Stefanovikio settlement with the location of scatterers that used for the correlation of subsidence/rainfall.

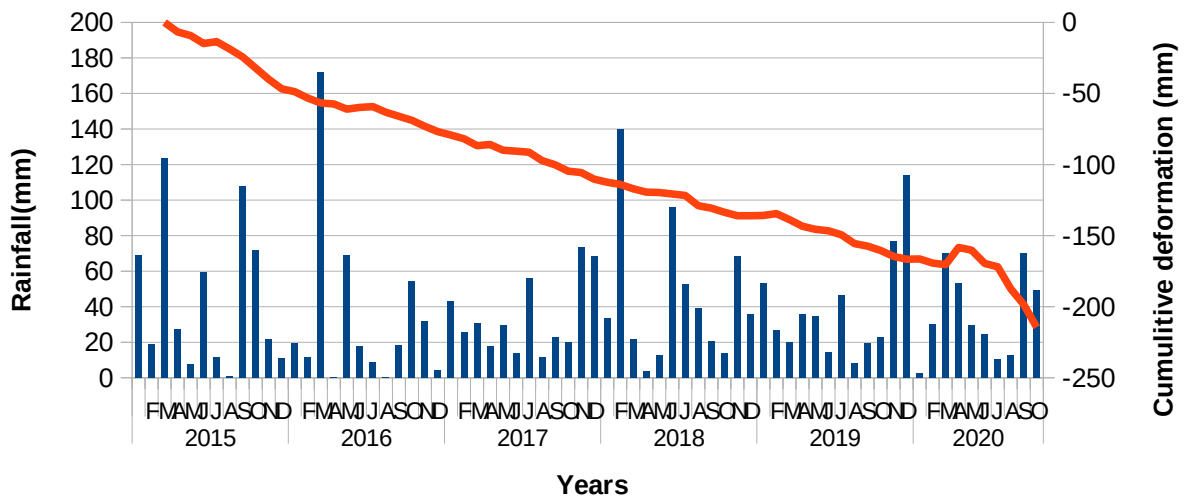
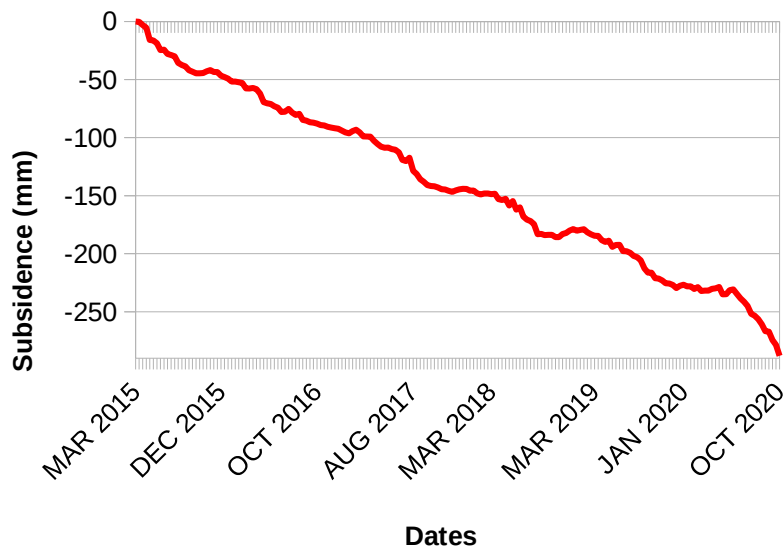


Figure 32: Time-Series plot of cumulative subsidence on Stefanovikio settlement (up). Cumulative times series correlated with rainfall data (down).

Further statistic analysis focuses on the seasonal effects on subsidence rates. In order to make a quantitative comparison we grouped the months based on their precipitations on dry (April to September) and wet seasons (October to March). After their separation into these categories, we calculated the cumulative subsidence and rainfall for every season (table 4). A scatter-plot (Figure 33) correlating these two parameters shows the great influence of precipitations on subsidence and the difference between the dry and wet seasons. As it was expected, dry seasons are characterized by higher cumulative subsidence. This result is more complex and it is not based only on the rainfall, nonetheless it is clear that higher subsidence

trends are expected on dry seasons. Bar-plot on Figure 34, displays the difference of subsidence between of dry and wet season of every year. According to the results, the 2019 is the year with the higher difference up to 33 mm.

Season	Start	End	Subsidence (mm)	Rainfall (mm)
Dry Season	Apr-15	Sept-15	- 39,95	214
Wet Season	Oct-15	Marc-16	-16,43	307
Dry Season	Apr-16	Sept-16	- 24,94	114
Wet Season	Oct-16	Marc-17	- 11,23	190
Dry Season	Apr-17	Sept-17	- 38,97	151
Wet Season	Oct-17	Marc-18	- 6,49	256
Dry Season	Apr-18	Sept-18	- 29,98	224
Wet Season	Oct-18	Marc-19	- 0,78	217
Dry Season	Apr-19	Sept-19	- 33,09	159
Wet Season	Oct-19	Marc-20	- 8,72	316
Dry Season	Apr-20	Sept-20	- 36,9	200

Table 4: Separation of months on dry - wet seasons based on precipitation. Cumulative subsidence and rainfall is calculated the for every season during the period 2015-2020 of Sentinel-1 vertical displacement product after displacement decomposition.

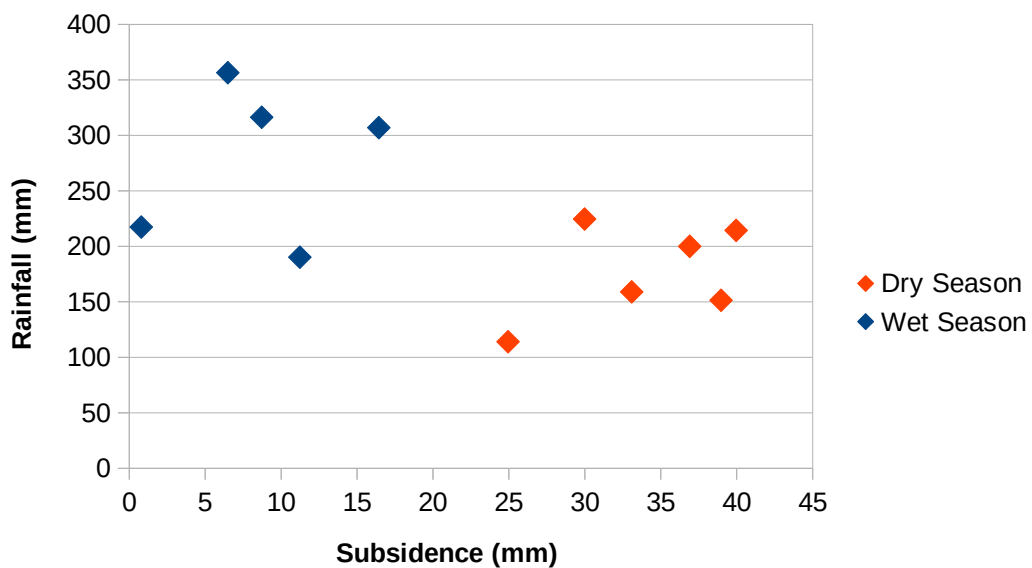


Figure 33: Scatter plot of rainfall-cumulative subsidence of dry-wet seasons during the period 2015-2020 of Sentinel-1 vertical displacement product after displacement decomposition.

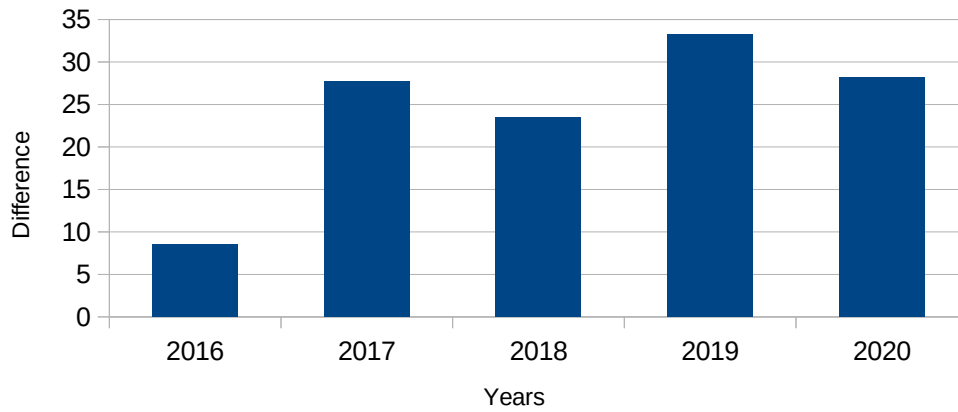
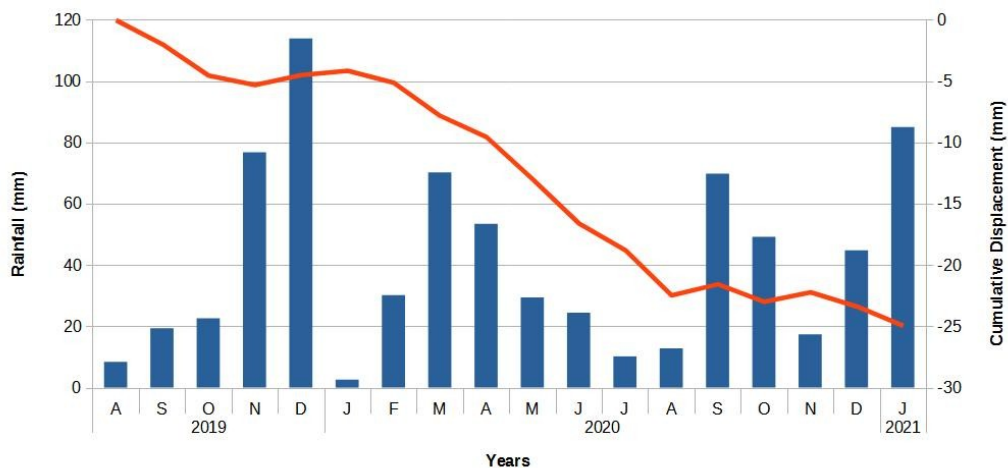
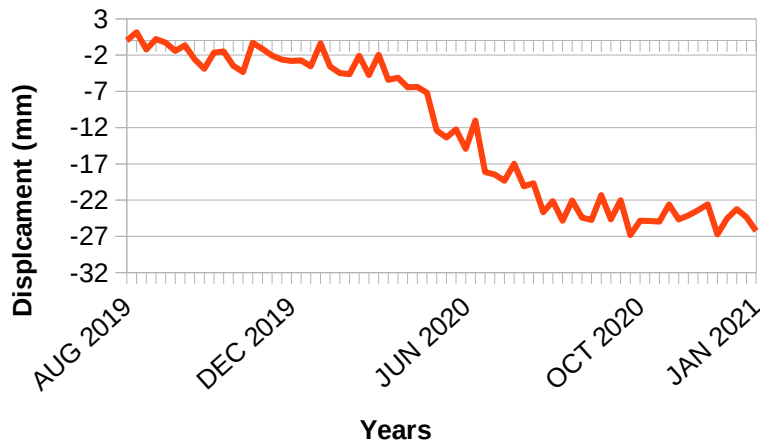


Figure 34: Subsidence rate difference between Dry – Wet season of every year for Sentinel-1. The highest difference is detected in 2019 (up to 33 mm).

Seasonal deformation signals are also detected on the Cosmo-SkyMed products. Bar-plot were generated to correlate these deformation pattern between the Stefanovikio settlement and rainfall of the study area. In Figure 35 the subsidence rates of Stefanovikio are increased on dry seasons as the precipitations decreased.



77 Figure 35: Time-Series plot of cumulative subsidence on Stefanovikio settlement (up).Cumulative times series correlated with rainfall data(down).

In Figure 36, time series of four settlements are showing the same subsidence patterns during the dry season. Higher difference can be detected on Kileler and Niki settlement. The locations of scatterers are visualized on the appendix. Focusing in the wet and dry season of Stefanovikio settlement (table 5) we see that the difference between the beginning and the end of wet season is up to 1-3 mm and 19 mm, for dry respectively. As the results of Sentinel-1, CSK data follows the same distribution on scatter-plot (Figure 37).

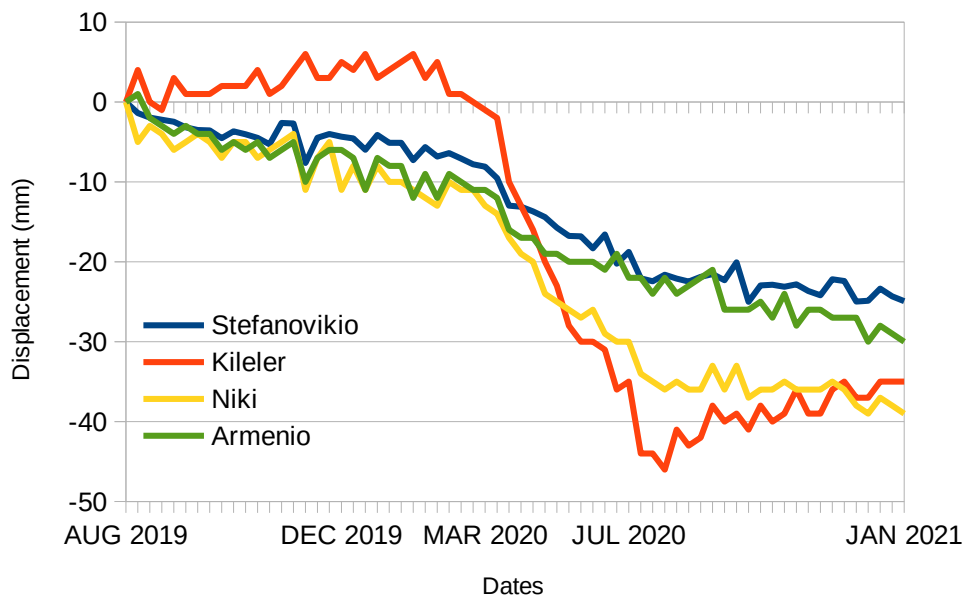


Figure 36: Time series of four settlements of Stefanovikio, Kileler, Niki and Armenio. The scatterers are located in areas with high subsidence trends.

Season	Start	End	Subsidence (mm)	Rainfall (mm)
Wet Season	Oct-19	Marc-20	-2,51	316
Dry Season	Apr-20	Sept-20	-19,63	200
Wet Season	Oct-20	Jan-21	-1,43	196

Table 5: Separation of months on dry - wet seasons based on precipitation. Cumulative subsidence and rainfall is calculated the for every season during the period 2019-2021 of CSK vertical displacement product generated by ascending geometry.

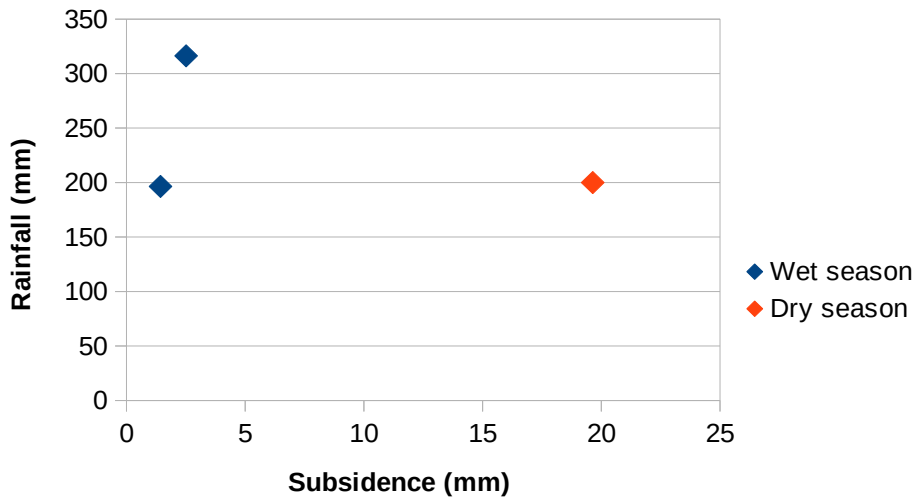


Figure 37: Scatter plot of rainfall-cumulative subsidence of dry-wet seasons during the period 2015-2020 CSK vertical displacement product generated by ascending geometry

Finally a comparison of subsidence rates between the two satellite systems was carried out focusing on Stefanovikio settlement (Figure 38). The results are showing that both satellites are following the same subsidence pattern over the wet and dry season of 2019 – 2020 with an interesting difference on wet season of 2020. Sentine-1 scatterers, beside the fact of higher precipitations during September and October of 2020, having a continuous subside while the CSK scatterers showing a stabilization of deformation which is expected due to the onset of the wet season.

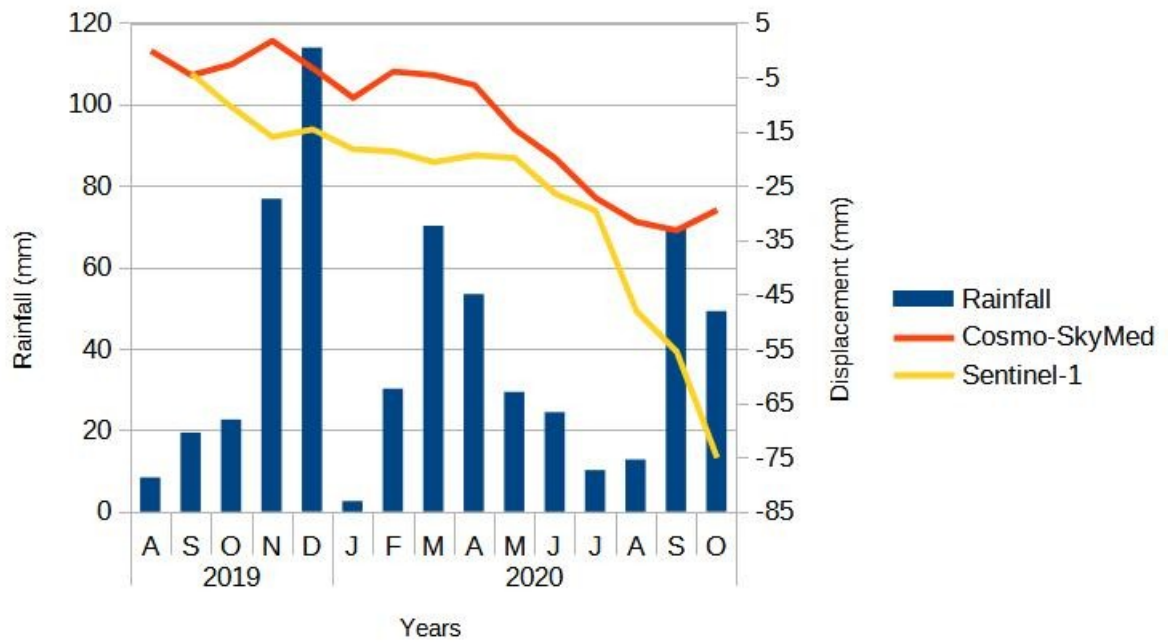


Figure 38: Comparison of CSK /Sentinel-1 subsidence rates, correlated with rainfall data covering the same period (Aug 2019 – Oct 2020).

8. Discussion - Conclusion

The main objectives of the current master dissertation concerns the update of previous studies on southern part of eastern Thessaly plain in order to investigate if there is potential decrease of land subsidence trend after the recharge of Karla lake in 2010 by generating multi-temporal interferometric products (deformation maps, cumulative deformation time-series) and correlate them with weather conditions of study area. Also, we had detect for first time the east-west movement of Larissa plain by generating displacement decomposition maps. The displacement products were produced by applying the SBAS algorithm on two different frequencies of SAR satellites (Sentinel-1, Cosmo-SkyMed).

The SBAS technique was applied to both geometries of Sentinel-1 data to detect and characterize the subsidence in Larissa plain. It was verified that Larissa plain continuous facing subsidence phenomena from 2015 to 2020 with the max subsidence trend at 123 mm/y for ascending and 95 mm/y for descending mode. The majority of scatterers are located in settlements, the main highway and the railroad. The significant subsidence was detected in the center of Larissa plain on the Armenio, Kileler and Achilio settlements as well as in the road-railway network close to them. Displacement decomposition shows that the max subsidence trend is up to 127 mm/y. Moreover detected the “opening” of the plain with small movements to east-west due to the active faults of Pliocene-Lower Pleistocene. The result seems to be reliable and consistent with previous studies. Comparing the results with previous studies shows a decrease of subsidence trend up to 3 – 5 cm/y which is possible caused by the recharge of Karla lake. It should be mentioned that the biggest changes on subsidence trend detected on Stefanovikio and Rizomilos settlements which are the closest to the lake, reinforcing the theory of groundwater recharge. Moreover the SBAS technique was applied in ascending mode of Cosmo-SkyMed data for a short period of time from 2019 to 2021. The generated products of average velocity trend show a subsidence up to -53 mm/y and a cumulative subsidence up to -65 mm located on infrastructures outside the Achilio settlement. The higher trends inside the settlements was detected on Kileler, Armenio and Stefanovikio reaching -34 to -52 mm/y . The results seem to qualitative agree with the subsidence pattern of Sentinel-1 products but with quantitative differences up to - 30 mm/y.

The pattern of the deformation indicates a combination of natural and anthropogenic causes related to climate change and groundwater irrigations. Climate change has increased in recent years by exponentially affecting average temperatures and reducing the frequency of rainfall resulting in a possible increase in dry periods. With the uncontrolled irrigation of groundwater for agriculture activities, the subsidence trend across the basin will continue causing greater damages to the urban and rural environment. According to the results of this study and the climate change predictions, strict measures must be taken by the local authorities to control irrigations through drillholes for the protection of groundwater reserves and consequently the decrease of subsidence trend. Future studies will focus on the impacts of land subsidence on critical infrastructures using geospatial intelligence methods, the historical meteorological data (30-40 years) from local stations to investigate long-term changes that could be linked to climate change and the predictions for future subsidence rates under the future rainfall conditions

From a technical point of view, the free access to huge archives of Copernicus SAR SLC data, contributes significantly to the intensive and more accurate monitoring of subsidence. The produced results have limited areas of low coherence (temporal and spatial decorrelation) on the urban environment of the settlements because Sentinel-1 exhibits high temporal resolution providing us information for larger areas.

In conclusion, according to the results of this study:

- Sentinel-1 products showing a land subsidence trend up to -95 to -130 mm/y. Higher subsidence values are detected in the center of the plain.
- Comparing the results of Sentinel-1 with previous studies, the land subsidence decreased (about 30 – 50 mm/y) but persists on southern Larissa plain.
- Cosmo-SkyMed products showing a land subsidence trend up to -50 mm/y following the same pattern with the Sentinel-1 displacement maps.
- The results seem to agree with the previous studies about the high subsidence rates in the dry seasons. As the dry periods are expecting to extent, larger subsidence rates will be detected.
- Opening of the plain detected on displacement decomposition shows that the normal faults activated during the Pliocene-Lower Pleistocene are still active affecting the geomorphology of SE Thessaly plain.

- Based on the meteorological data of our study period (2015-2020), the precipitation and mean temperatures are stable showing no changes. Although, dry and wet seasons having an important role on subsidence trending. As the climate change is going to change those parameters, it is possible to increase the subsidence rates. Strict measurements must be taken in order to control the illegal irrigation (drill holes).
- Future studies will focus on the impact of subsidence on critical infrastructures and analyze the seasonal deformation patterns.
- Finally according to the results of this study, the recharge of Karla lake has an impact on the ground-water deposits as a result the decrease of land subsidence rates on settlements close to lake. The main problem of subsidence is located on the center of the plain with higher trends comparing with previews research.

Reference

Andreas, H., Zainal Abidin, H., Pradipta, D., Anggreni Sarsito, D., & Gumilar, I. (2018). *Insight look the subsidence impact to infrastructures in Jakarta and Semarang area; Key for adaptation and mitigation. MATEC Web of Conferences, 147, 08001.* doi:10.1051/mateconf/201814708001

Argyrikis, P., Ganas, A., Valkaniotis, S., Tsioumas, V., Sagias, N., & Psiloglou, B. (2020). *Anthropogenically induced subsidence in Thessaly, central Greece: new evidence from GNSS data. Natural Hazards.*doi:10.1007/s11069-020-03917-w

Benekos G., Derdelakos K. , Bountzouklis Ch. , Parcharidis I., (2014). Monitoring the subsidence in the plain of south Thessaly with SAR Inteferometry . Conference: 10th Int. Congress of the Hellenic Geographical Society,Thessaloniki, Greece

Berardino, P., Fornaro, G., Lanari, R., & Sansosti, E. (2002). *A new algorithm for surface deformation monitoring based on small baseline differential SAR interferograms. IEEE Transactions on Geoscience and Remote Sensing, 40(11), 2375–2383.* doi:10.1109/tgrs.2002.803792

Cigna, F., & Tapete, D. (2020). *Present-day land subsidence rates, surface faulting hazard and risk in Mexico City with 2014–2020 Sentinel-1 IW InSAR. Remote Sensing of Environment, 112161.*doi:10.1016/j.rse.2020.112161

EUROPEAN SPACE AGANCY., InSAR Principles: Guidelines for SAR Interferometry Processing and Interpretation (ESA TM-19), accessed 14 January 2021 <https://www.esa.int/About_Us/ESA_Publications/InSAR_Principles_Guidelines_for_SAR_Interferometry_Processing_and_Interpretation_br_ESA_TM-19>

Fattahi, H., & Amelung, F. (2013). *DEM Error Correction in InSAR Time Series. Geoscience and Remote Sensing, IEEE Transactions On, 51(7), 4249–4259.* doi:10.1109/tgrs.2012.2227761

Ferretti, A., (2014). Satellite InSAR data: reservoir monitoring from space. EAGE Publications.

Ferretti, A., Monti Guarnieri, A., Prati, C., & Rocca, F., 1997. Multi-baseline interferometric techniques and applications. In ERS SAR Interferometry (Vol. 406, p. 243)

Foumelis, M., Papageorgiou, E., & Stamatopoulos, C. (2016). *Episodic ground deformation signals in Thessaly Plain (Greece) revealed by data mining of SAR interferometry time series. International Journal of Remote Sensing, 37(16), 3696–3711.* doi:10.1080/01431161.2016.1201233

Fialko Y., Simons M., 2001. *The complete (3-D) surface displacement in the epicentral area of the 1999 Mw 7.1 Hector Mine earthquake, California, from space geodetic observations. Geophysical Research Letters, vol. 28, no 16, pp 3063-3066.*

Fylaktos, A., Parcharidis, I., (2019). Updating of surface subsidence using SAR interferometry after counter measures by activating an old reservoir for water consuming control, Living Planet Symposium, 13-17 May, Milan, Italy

Gabriel, A. K., Goldstein, R. M., & Zebker, H. A., 1989. Mapping small elevation changes over large areas: differential radar interferometry. *Journal of Geophysical Research: Solid Earth*, 94(B7), 9183-9191. Drury, S. A., 1987. Image interpretation in geology.

Giannakopoulos, C., Kostopoulou, E., Varotsos, K. V., Tziotziou, K., & Plitharas, A. (2011). *An integrated assessment of climate change impacts for Greece in the near future. Regional Environmental Change, 11(4), 829–843.* doi:10.1007/s10113-011-0219-8

Global climate Change: Vital Signs of the Planet., The Causes of climate Change, accessed 25 January 2021, <<https://climate.nasa.gov/causes/>>

Hu, B., Yang, B., Zhang, X., Chen, X., & Wu, Y. (2019). *Time-Series Displacement of Land Subsidence in Fuzhou Downtown, Monitored by SBAS-InSAR Technique. Journal of Sensors, 2019, 1–12.* doi:10.1155/2019/3162652

International Groundwater Resources Assessment Centre (IGRAC), Groundwater & climate Change, accessed 30 January 2021, <<https://www.un-igrac.org/areas-expertise/groundwater-climate-change>>

Kaplanides A, Fountoulis D (1997). Subsidence phenomena and ground fissures in Larissa, Karla basin, Greece: their results in urban and rural environment. In: Marinos P, Koukis G, Tsiambaos G, Sambatakakis G (eds) *Eng Geol Environ*. Balkema, Rotterdam, pp 729–735

Kontogianni, V., Pytharouli, S., & Stiros, S. (2006). *Ground subsidence, Quaternary faults and vulnerability of utilities and transportation networks in Thessaly, Greece. Environmental Geology*, 52(6), 1085–1095. doi:10.1007/s00254-006-0548-y

Lanari, R., Casu, F., Manzo, M., Zeni, G., Berardino, P., Manunta, M., & Pepe, A. (2007). An Overview of the Small Baseline Subset Algorithm: A DInSAR Technique for Surface Deformation Analysis. *Deformation and Gravity Change: Indicators of Isostasy, Tectonics, Volcanism, and climate Change*, 637–661. doi:10.1007/978-3-7643-8417-3_2

Lanari, R., Mora, O., Manunta, M., Mallorqui, J. J., Berardino, P., & Sansosti, E. (2004). *A small-baseline approach for investigating deformations on full-resolution differential SAR interferograms. IEEE Transactions on Geoscience and Remote Sensing*, 42(7), 1377–1386. doi:10.1109/tgrs.2004.828196

Loukas, A., & Vasiliades, L. (2004). *Probabilistic analysis of drought spatiotemporal characteristics in Thessaly region, Greece. Natural Hazards and Earth System Science*, 4(5/6), 719–731. doi:10.5194/nhess-4-719-2004

Miranda, N., Rosich, B., Santella, C., & Grion, M., 2003. Review of the impact of ERS-2 piloting modes on the SAR Doppler stability. *Proceedings Fringe '03*, 1-5

Ng, A. H.-M., Ge, L., Zhang, K., Chang, H.-C., Li, X., Rizos, C., & Omura, M. (2011). *Deformation mapping in three dimensions for underground mining using InSAR – Southern highland coalfield in New South Wales, Australia. International Journal of Remote Sensing*, 32(22), 7227–

7256. doi:10.1080/01431161.2010.519741

Osmanoğlu, B., Sunar, F., Wdowinski, S., & Cabral-Cano, E., (2016). Time series analysis of InSAR data: Methods and trends. *ISPRS Journal of Photogrammetry and Remote Sensing*, 115, 90-102.

Parcharidis, I., Fomelis, M. & Katsafados, P., (2011). Seasonal ground deformation monitoring over Southern Larissa Plain (Central Greece) by SAR interferometry, In: *Advances in the Research of Aquatic Environment*, N. Lambrakis, G. Stournaras & K. Katsanou (eds), *Environmental Earth Sciences*, Springer, vol. 2, 497-504.

Pawluszek-Filipiak, K., & Borkowski, A. (2020). *Integration of DInSAR and SBAS Techniques to Determine Mining-Related Deformations Using Sentinel-1 Data: The Case Study of Rydułtowy Mine in Poland. Remote Sensing*, 12(2), 242. doi:10.3390/rs12020242

Reichenmiller, P., (2011). The hidden risks of climate change: an increase in property damage from soil subsidence in Europe. Swiss Re publications.

Touzi, R., Lopes, A., Bruniquel, J., & Vachon, P. W., (1999). Coherence estimation for SAR imagery. *IEEE Transactions on Geoscience and Remote Sensing*, 37(1), 135-149.

U.S. Geological Survey., InSAR—Satellite-based technique captures overall deformation "picture", accessed 25 January 2021, <<https://www.usgs.gov/natural-hazards/volcano-hazards/insar-satellite-based-technique-captures-overall-deformation-picture>>

Zebker, H. A., & Villasenor, J., (1992). Decorrelation in interferometric radar echoes. *IEEE Transactions on geoscience and remote sensing*, 30(5), 950-959.

Zebker, H. A., & Goldstein, R. M. (1986). *Topographic mapping from interferometric synthetic aperture radar observations. Journal of Geophysical Research*, 91(B5), 4993. doi:10.1029/jb091ib05p04993

Appendix

Acquisition	Orbit	Date	Polarization	Geometry
1	102	20150305	VV	Ascending
2	102	20150329	VV	Ascending
3	102	20150410	VV	Ascending
4	102	20150422	VV	Ascending
5	102	20150516	VV	Ascending
6	102	20150528	VV	Ascending
7	102	20150609	VV	Ascending
8	102	20150703	VV	Ascending
9	102	20150727	VV	Ascending
10	102	20150820	VV	Ascending
11	102	20150901	VV	Ascending
12	102	20150925	VV	Ascending
13	102	20151112	VV	Ascending
14	102	20151218	VV	Ascending
15	102	20160111	VV	Ascending
16	102	20160216	VV	Ascending
17	102	20160228	VV	Ascending
18	102	20160323	VV	Ascending
19	102	20160416	VV	Ascending
20	102	20160510	VV	Ascending
21	102	20160603	VV	Ascending
22	102	20160709	VV	Ascending
23	102	20160721	VV	Ascending
24	102	20160802	VV	Ascending
25	102	20160826	VV	Ascending
26	102	20161001	VV	Ascending
27	102	20161031	VV	Ascending
28	102	20161118	VV	Ascending
29	102	20161206	VV	Ascending
30	102	20161230	VV	Ascending
31	102	20170105	VV	Ascending
32	102	20170123	VV	Ascending
33	102	20170204	VV	Ascending
34	102	20170228	VV	Ascending
35	102	20170306	VV	Ascending
36	102	20170330	VV	Ascending
37	102	20170411	VV	Ascending
38	102	20170429	VV	Ascending
39	102	20170505	VV	Ascending
40	102	20170529	VV	Ascending
41	102	20170604	VV	Ascending
42	102	20170628	VV	Ascending
43	102	20170710	VV	Ascending
44	102	20170722	VV	Ascending
45	102	20170803	VV	Ascending
46	102	20170827	VV	Ascending

47	102	20170902	VV	Ascending
48	102	20170926	VV	Ascending
49	102	20171002	VV	Ascending
50	102	20171020	VV	Ascending
51	102	20171101	VV	Ascending
52	102	20171125	VV	Ascending
53	102	20171201	VV	Ascending
54	102	20171231	VV	Ascending
55	102	20180106	VV	Ascending
56	102	20180130	VV	Ascending
57	102	20180205	VV	Ascending
58	102	20180217	VV	Ascending
59	102	20180301	VV	Ascending
60	102	20180331	VV	Ascending
61	102	20180406	VV	Ascending
62	102	20180424	VV	Ascending
63	102	20180512	VV	Ascending
64	102	20180530	VV	Ascending
65	102	20180705	VV	Ascending
66	102	20180729	VV	Ascending
67	102	20180810	VV	Ascending
68	102	20180822	VV	Ascending
69	102	20180903	VV	Ascending
70	102	20180927	VV	Ascending
71	102	20181003	VV	Ascending
72	102	20181027	VV	Ascending
73	102	20181102	VV	Ascending
74	102	20181202	VV	Ascending
75	102	20181226	VV	Ascending
76	102	20190107	VV	Ascending
77	102	20190113	VV	Ascending
78	102	20190212	VV	Ascending
79	102	20190218	VV	Ascending
80	102	20190302	VV	Ascending
81	102	20190326	VV	Ascending
82	102	20190401	VV	Ascending
83	102	20190419	VV	Ascending
84	102	20190501	VV	Ascending
85	102	20190525	VV	Ascending
86	102	20190606	VV	Ascending
87	102	20190630	VV	Ascending
88	102	20190706	VV	Ascending
89	102	20190730	VV	Ascending
90	102	20190805	VV	Ascending
91	102	20190829	VV	Ascending
92	102	20190904	VV	Ascending
93	102	20190928	VV	Ascending
94	102	20191016	VV	Ascending
95	102	20191028	VV	Ascending
96	102	20191103	VV	Ascending

97	102	20191127	VV	Ascending
98	102	20191209	VV	Ascending
99	102	20191227	VV	Ascending
100	102	20200108	VV	Ascending
101	102	20200126	VV	Ascending
102	102	20200201	VV	Ascending
103	102	20200225	VV	Ascending
104	102	20200302	VV	Ascending
105	102	20200326	VV	Ascending
106	102	20200425	VV	Ascending
107	102	20200501	VV	Ascending
108	102	20200531	VV	Ascending
109	102	20200612	VV	Ascending
110	102	20200618	VV	Ascending
111	102	20200630	VV	Ascending
112	102	20200706	VV	Ascending
113	102	20200730	VV	Ascending
114	102	20200811	VV	Ascending
115	102	20200817	VV	Ascending
116	102	20200829	VV	Ascending
117	102	20200904	VV	Ascending
118	102	20200922	VV	Ascending
119	102	20201004	VV	Ascending
120	102	20201022	VV	Ascending
121	7	20150311	VV	Descending
122	7	20150404	VV	Descending
123	7	20150428	VV	Descending
124	7	20150627	VV	Descending
125	7	20150709	VV	Descending
126	7	20150721	VV	Descending
127	7	20150802	VV	Descending
128	7	20150826	VV	Descending
129	7	20150907	VV	Descending
130	7	20150919	VV	Descending
131	7	20151001	VV	Descending
132	7	20151025	VV	Descending
133	7	20151212	VV	Descending
134	7	20151224	VV	Descending
135	7	20160129	VV	Descending
136	7	20160210	VV	Descending
137	7	20160305	VV	Descending
138	7	20160329	VV	Descending
139	7	20160516	VV	Descending
140	7	20160528	VV	Descending
141	7	20160609	VV	Descending
142	7	20160703	VV	Descending
143	7	20160727	VV	Descending
144	7	20160808	VV	Descending
145	7	20160820	VV	Descending
146	7	20160901	VV	Descending

147	7	20160925	VV	Descending
148	7	20161019	VV	Descending
149	7	20161031	VV	Descending
150	7	20161112	VV	Descending
151	7	20161124	VV	Descending
152	7	20161206	VV	Descending
153	7	20161230	VV	Descending
154	7	20170111	VV	Descending
155	7	20170123	VV	Descending
156	7	20170204	VV	Descending
157	7	20170228	VV	Descending
158	7	20170306	VV	Descending
159	7	20170324	VV	Descending
160	7	20170423	VV	Descending
161	7	20170429	VV	Descending
162	7	20170511	VV	Descending
163	7	20170523	VV	Descending
164	7	20170604	VV	Descending
165	7	20170628	VV	Descending
166	7	20170710	VV	Descending
167	7	20170722	VV	Descending
168	7	20170803	VV	Descending
169	7	20170827	VV	Descending
170	7	20170908	VV	Descending
171	7	20170920	VV	Descending
172	7	20171008	VV	Descending
173	7	20171020	VV	Descending
174	7	20171107	VV	Descending
175	7	20171125	VV	Descending
176	7	20171213	VV	Descending
177	7	20171225	VV	Descending
178	7	20180106	VV	Descending
179	7	20180130	VV	Descending
180	7	20180205	VV	Descending
181	7	20180223	VV	Descending
182	7	20180313	VV	Descending
183	7	20180331	VV	Descending
184	7	20180412	VV	Descending
185	7	20180424	VV	Descending
186	7	20180512	VV	Descending
187	7	20180530	VV	Descending
188	7	20180611	VV	Descending
189	7	20180705	VV	Descending
190	7	20180717	VV	Descending
191	7	20180810	VV	Descending
192	7	20180822	VV	Descending
193	7	20180903	VV	Descending
194	7	20180927	VV	Descending
195	7	20181009	VV	Descending
196	7	20181027	VV	Descending

197	7	20181102	VV	Descending
198	7	20181114	VV	Descending
199	7	20181208	VV	Descending
200	7	20181226	VV	Descending
201	7	20190119	VV	Descending
202	7	20190212	VV	Descending
203	7	20190224	VV	Descending
204	7	20190302	VV	Descending
205	7	20190326	VV	Descending
206	7	20190407	VV	Descending
207	7	20190419	VV	Descending
208	7	20190501	VV	Descending
209	7	20190531	VV	Descending
210	7	20190606	VV	Descending
211	7	20190624	VV	Descending
212	7	20190706	VV	Descending
213	7	20190730	VV	Descending
214	7	20190805	VV	Descending
215	7	20190829	VV	Descending
216	7	20190910	VV	Descending
217	7	20190922	VV	Descending
218	7	20191016	VV	Descending
219	7	20191028	VV	Descending
220	7	20191103	VV	Descending
221	7	20191127	VV	Descending
222	7	20191209	VV	Descending
223	7	20191227	VV	Descending
224	7	20200108	VV	Descending
225	7	20200120	VV	Descending
226	7	20200201	VV	Descending
227	7	20200225	VV	Descending
228	7	20200302	VV	Descending
229	7	20200320	VV	Descending
230	7	20200407	VV	Descending
231	7	20200413	VV	Descending
232	7	20200425	VV	Descending
233	7	20200507	VV	Descending
234	7	20200531	VV	Descending
235	7	20200612	VV	Descending
236	7	20200630	VV	Descending
237	7	20200706	VV	Descending
238	7	20200730	VV	Descending
239	7	20200811	VV	Descending
240	7	20200823	VV	Descending
241	7	20200904	VV	Descending
242	7	20200922	VV	Descending
243	7	20201010	VV	Descending
244	7	20201022	VV	Descending

Acquisition	Satellite	Date	Polarization
1	CSKS2	20190817	HH
2	CSKS3	20190829	HH
3	CSKS4	20190901	HH
4	CSKS2	20190902	HH
5	CSKS1	20190910	HH
6	CSKS2	20190918	HH
7	CSKS1	20190926	HH
8	CSKS3	20190930	HH
9	CSKS4	20191003	HH
10	CSKS4	20191019	HH
11	CSKS1	20191028	HH
12	CSKS3	20191101	HH
13	CSKS4	20191104	HH
14	CSKS4	20191120	HH
15	CSKS2	20191121	HH
16	CSKS1	20191129	HH
17	CSKS4	20191206	HH
18	CSKS2	20191207	HH
19	CSKS1	20191215	HH
20	CSKS1	20191231	HH
21	CSKS2	20200108	HH
22	CSKS1	20200116	HH
23	CSKS4	20200123	HH
24	CSKS1	20200201	HH
25	CSKS3	20200205	HH
26	CSKS2	20200209	HH
27	CSKS1	20200217	HH
28	CSKS3	20200221	HH
29	CSKS4	20200224	HH
30	CSKS1	20200304	HH
31	CSKS1	20200320	HH
32	CSKS1	20200405	HH
33	CSKS3	20200511	HH
34	CSKS4	20200514	HH
35	CSKS2	20200531	HH
36	CSKS4	20200615	HH
37	CSKS1	20200624	HH
38	CSKS3	20200628	HH
39	CSKS4	20200701	HH
40	CSKS2	20200702	HH
41	CSKS1	20200710	HH
42	CSKS3	20200714	HH
43	CSKS4	20200717	HH
44	CSKS1	20200726	HH
45	CSKS4	20200802	HH
46	CSKS1	20200811	HH
47	CSKS3	20200815	HH
48	CSKS4	20200818	HH
49	CSKS1	20200827	HH

50	CSKS1	20200912	HH
51	CSKS3	20200916	HH
52	CSKS4	20200919	HH
53	CSKS1	20200928	HH
54	CSKS4	20201005	HH
55	CSKS2	20201006	HH
56	CSKS1	20201014	HH
57	CSKS3	20201018	HH
58	CSKS4	20201021	HH
59	CSKS2	20201022	HH
60	CSKS2	20201107	HH
61	CSKS1	20201115	HH
62	CSKS3	20201119	HH
63	CSKS4	20201208	HH
64	CSKS1	20201217	HH
65	CSKS4	20201224	HH
66	CSKS1	20210102	HH

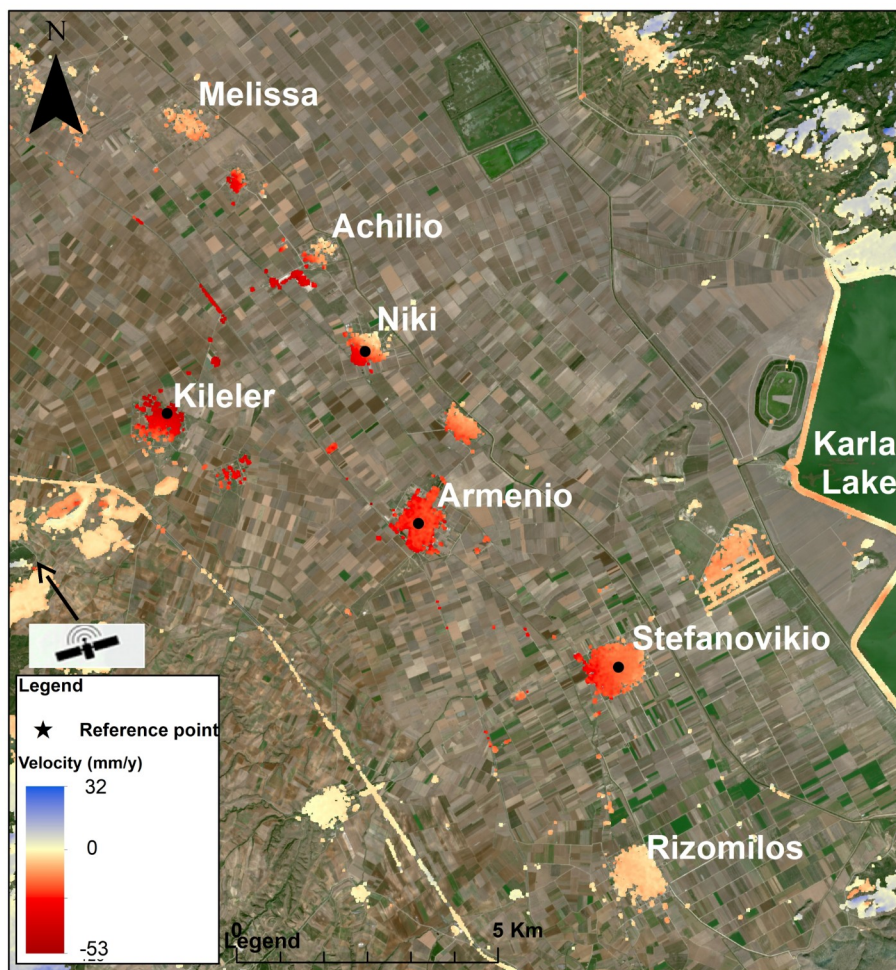


Figure 39: Locations of scatterers of CSK data that used for time-series plots.